Segmented lateral dyke growth in a rifting event at Bárðarbunga volcanic system, Iceland

Freysteinn Sigmundsson[1], Andrew Hooper[2], Sigrún Hreinsdóttir[3], Kristín S. Vogfjörd[4], Benedikt Ófeigsson[4], Elías Rafn Heimisson[1], Stéphanie Dumont[1], Michelle Parks[1], Karsten Spaans[2], Gunnar B. Guðmundsson[4], Vincent Drouin[1], Thóra Árnadóttir[1], Kristín Jónsdóttir[4], Magnús T. Gudmundsson[1], Thórdís Högnadóttir[1], Hildur María Friðriksdóttir[1+4], Martin Hensch[4], Páll Einarsson[1], Eyjólfur Magnússon[1], Sergey Samsonov[5], Bryndís Brandsdóttir[1], Robert S. White[6], Thorbjörg Ágústsdóttir[6], Timothy Greenfield[6], Robert G. Green[6], Ásta Rut Hjartardóttir[1], Rikke Pedersen[1], Rick Bennett[7], Halldór Geirsson[8], Pete LaFemina[8], Helgi Björnsson[1], Finnur Pálsson[1], Erik Sturkell[9], Christopher J. Bean[10], Martin Möllhoff[10], Aoife Braiden[10], and Eva P.S. Eibl[10]

[1] Nordic Volcanological Center, Institute of Earth Sciences, University of Iceland, IS-101 Reykjavík, Iceland

[2] COMET, School of Earth and Environment, University of Leeds, Leeds, LS2 9JT, UK

[3] GNS Science, Avalon 5010, Lower Hutt, New Zealand

[4] Icelandic Meteorological Office, IS-150 Reykjavík, Iceland

[5] Canada Centre for Mapping and Earth Observation, Natural Resources Canada, 560 Rochester Street, Ottawa, ON K1A 0E4 Canada

[6] Dept. Earth Sciences, University of Cambridge, Madingley Road, Cambridge CB3

0EZ, UK

[7] University of Arizona, Tucson, Arizona 85721, USA

[8] The Pennsylvania State University, University Park, Pennsylvania 16802, USA

[9] University of Gothenburg, SE-405 30 Gothenburg, Sweden

[10] Seismology Laboratory, School of Geological Sciences, University College Dublin, Belfield, Dublin 4, Ireland

First paragraph + main text (2461 words / max ~2350 words)

Crust at many divergent plate boundaries forms primarily by the injection of vertical sheet-like dykes, some tens of km long[1]. Previous models of rifting events indicate either a lateral dyke growth away from a feeding source, with propagation rates decreasing as the dyke lengthens[2,3,4], or magma flowing vertically into dykes from an underlying source[5,6], with the role of topography on the evolution of lateral dykes not clear. Here we show how a recent segmented dyke intrusion in the Bárðarbunga volcanic system, grew laterally for over 45 km at a variable rate, with an influence of topography on the direction of propagation. Barriers at the ends of each segment were overcome by the build-up of pressure in the dyke end; then a new segment formed and dyke lengthening temporarily peaked. The dyke evolution, which occurred over 14 days, was revealed by propagating seismicity, ground deformation mapped by Global Positioning System (GPS), interferometric analysis of satellite radar

images (InSAR), and graben formation. The strike of the dyke segments varies from an initially radial direction away from the Bárðarbunga caldera, towards alignment with that expected from regional stress at the distal end. A model minimizing the combined strain and gravitational potential energy explains the propagation path. Dyke opening and seismicity focused at the most distal segment at any given time, and were simultaneous with a magma source deflation and slow collapse at the Bárðarbunga caldera, accompanied by a series of M>5 earthquakes. The dyke growth was slowed down by an effusive fissure eruption near the end of the dyke. Lateral dyke growth with segment barrier breaking by pressure build-up in the dyke distal end explains how focused upwelling of magma under central volcanoes is effectively redistributed over long distances to create new upper crust at divergent plate boundaries.

The formation of dykes is favourable at divergent plate boundaries as plate movements stretch the crust and reduce the normal stress on potential dyke planes. Rifting events at divergent plate boundaries typically occur in episodes separated by hundreds of years of quiescence. Only a few such episodes have been monitored, as most divergent plate boundaries form mid-ocean ridges. In 1975-1984 a rifting episode took place at Krafla volcano, Iceland and from 2005-2010 in the Afar region of Ethiopia[1]. Limited geodetic and seismic data have been interpreted in terms of lateral flow of magma with dyke propagation rates initially of up to two to three km per day, and then at a declining rate as magma propagates away from a central feeding source[2,3,4]. The propagation of such dykes has been modelled as inflation of magma filled cracks with uniform excess pressure[7,8]. The formation of regional dykes

in Iceland has alternatively been attributed to the vertical rise of magma from major magma reservoirs underlying dyke swarms[5,6].

Bárðarbunga is a subglacial basaltic central volcano with a 70 km^2 caldera at the northwestern corner of Vatnajökull ice cap in Iceland[9,10] (Fig. 1, Extended Data item 1). It has an associated fissure swarm[11] extending 115 km to the SW and 55 km to the NNE. Activity in the last 2000 years includes both subglacial eruptions as well as major effusive fissure eruptions, with 23 verified eruptions in the last 1100 years[12]. Timings of the most recent effusive eruptions north of the Vatnajökull ice cap, originating from the Bárðarbunga system, are not well known, but they are inferred to have produced the Holuhraun lava field sometime in the period from 1794 to 1864[6]. The Holuhraun eruptive fissure was reactivated in 2014. In 1996, the Gjálp subglacial eruption was likely triggered by the Bárðarbunga volcanic system[13,14]. Since 2005 seismic activity at Bárðarbunga has been steadily increasing, mostly confined to the area NE of its caldera.

On 16 August 2014 at 03:00 UTC an intense seismic swarm began at Bárðarbunga. Initial seismic activity occurred in several clusters. One cluster was consistent with the formation of a radial dyke segment aligned in direction N127°E outward from the Bárðarbunga caldera. Other clusters to the NW of the caldera may also signify magma movements, or stress induced seismicity. GPS observations show simultaneous deflation of the caldera and displacements consistent with widening across the N127°E radial dyke, although deformation due to magma movements in the other clusters may also contribute. The seismic activity then focused on a lineament in direction N55°E, extending from the southern tip of the initial N127°E dyke segment (Extended Data item 2). Lateral growth of this dyke is reflected in the

migration of seismicity, along segments of variable strike; maximum widening of 1.3 m occurred between stations URHC and KVER spaced 25 km apart (Supplementary Fig. 1). Displacements of continuous GPS stations indicate the fastest rate of widening at any time in the most distal segment of the dyke throughout its evolution. The rate of dyke propagation varied considerably. A long halt in propagation for 80 hours began on 19 August. Propagation rate exceeded 1 km/hour on 23 August when a new segment initiated with a 90° left turn and advanced 4 km NNW over two short segments. Following this the dyke took a right turn onto a new lineament striking N47°E, and then onto a N25°E striking segment.

The lengthening of the dyke ended on 27 August around 10 km north of Vatnajökull and a minor fissure erupted in Holuhraun for about 4 hours on 29 August. On 31 August a new eruption began from the same fissure and is still ongoing at the time of writing. After 4 September the movement associated with the dyke was minor, suggesting an approximate equilibrium between inflow of magma into the dyke and magma flowing out of it feeding the eruption. Minor eruptions may have occurred under Vatnajökull; shallow ice depressions marked by circular crevasses (ice cauldrons) were discovered in the period 27/08-07/09, indicating leakage of magma or magmatic heat to the glacier causing basal melting (Fig. 1 and 2b). On 5 September, aircraft radar profiling showed that the ice surface in the centre of the Bárðarbunga caldera had subsided 16 m relative to the surroundings, resulting in a 0.32 ± 0.08 km^3 subsidence bowl (Fig. 1, Extended Data item 3). No evidence for basal melting was observed inside the caldera suggesting subsidence of the caldera floor. This slow collapse of the caldera floor is considered to have started between August 16 (start of unrest) and August 24 (beginning of a series of M≥5 earthquakes

in the caldera), with up to 0.8-1.2 m/day average rate of subsidence in this period. It can be compared to a 1 day interferogram over the ice surface spanning 27 -28 August (Fig. 1), that has maximum line-of-sight (LOS) increase of 57 cm, indicating 55-70 cm of subsidence, during 24 hours. From 24 August to 6 September 16 M≥5 earthquakes occurred on the caldera boundary.

Over 22000 earthquakes were automatically detected 16/08-06/09 2014, 5000 of which have been manually checked. Four thousand of these have been relatively relocated, defining the dyke segments. Ground deformation in areas outside the Vatnajökull ice cap, and on nunataks within the ice cap, is well mapped by a combination of InSAR, continuously recording GPS sites, and campaign GPS measurements. The GPS observations and analysis give the temporal evolution of the three-dimensional displacements used in the modelling (Fig. 1). Interferometric analysis of synthetic aperture radar images from the COSMO-SkyMed, RADARSAT-2 and TerraSAR-X satellites was used to form 11 interferograms showing LOS change spanning different time intervals (Supplementary Fig. 2). The analysis of seismic and geodetic data is described in Methods.

Initial modelling of the dyke, with no *a priori* constraints on position, strike or dip, show the deformation data require the dyke to be approximately vertical and line up with the seismicity (Extended Data item 4). We therefore fixed the dip to be vertical and the lateral position of the dyke to coincide with the earthquake locations. We modelled the dyke as a series of rectangular patches and estimated the opening and slip on each patch (Fig. 3a; see Supplementary Figures 3-4 for slip and standard deviations of opening). We used a Markov-chain Monte Carlo approach to estimate

the multivariate probability distribution for all model parameters (Methods) on each day 16/08-06/09 2014 (Fig. 2d). The results suggest that most of the magma injected into the dyke is shallower than the seismicity, which mostly spans the depth range from 5 to 8 km below sea level (see Fig. 2c and Methods). While magma may extend to depths greater than 9 km near the centre of the ice cap, towards the edge of the ice cap where constraints from InSAR and GPS are much better, significant opening is all shallower than 5 km (Fig. 3a). The total volume intruded into the dyke by 28 August was 0.48-0.51 km^3.

We took two approaches to deflation models: (i) by combining GPS displacements on 04/09, interferograms ending on 03/09 and 04/09, respectively, and the caldera subsidence measured on 05/09, and (ii) by combining all data except the caldera subsidence in a time dependent model. Our approximate model has two dip-slip faults at the boundary of the caldera and an underlying magma source; either a spherical or a flat top chamber. In approach (i) the best-fit models have a spherical chamber centred at 1.3-1.5 km depth below sea level and volume change of 0.26-0.29 km^3, or a flat-topped chamber stretching from 3.4-3.6 km downwards and volume change of 0.24-0.31 km^3 (Extended Data items 5 and 6, Supplementary Figs. 5 and 6). We consider the actual volume loss at depth to be at least equal to the volume of the caldera subsidence on 05/09 (0.32±0.08 km^3); the volumes predicted by our simple models are marginally smaller. The time dependent models not using the caldera subsidence result in under-prediction of the volume change. Inverting the GPS and InSAR data from 03/09 and 04/09, but neglecting the caldera subsidence measurements, results in a volume change that is smaller by a factor of 2.0. We therefore scale the estimated volumes in our time dependent models by this factor to

give more reliable estimate (Fig. 4). The volume decrease beneath the caldera tracks

the volume increase of the dyke for the first week of the activity. The volume

decrease then decelerates to less than half the previous rate, although the dyke volume

increase continues at the same rate. This suggests inflow of magma from an

underlying deeper source after the first week, which is not visible in the geodetic data.

Full details of the results are given in Methods and Supplementary Information.

Lateral growth of a dyke is expected to follow the minimum potential energy

principle. Assuming a closed system, a dyke will tend to be emplaced such that it

minimizes the total potential energy[15,16,17], Θ_T, equal to:

(1) $$\Theta_T = \Theta_s + \Theta_g$$

where Θ_s is the strain potential and Θ_g the gravitational energy potential. Evaluation

of the strain energy requires knowledge of the prior stress and strain field in the crust.

We consider here the role of plate movements and topography in steering the

propagation path of a dyke once it is initiated; its onset point will depend on other

factors such as details of the magma plumbing system feeding it and the path of

previous dykes. We approximate strain and stress due to plate movements as

described in Methods, and then consider strain changes induced by the dyke

formation. Opening of a dyke is energetically favourable when it releases strain

energy built up at a divergent plate boundary, but once deviatoric stress in the crust

adjacent to a segment is released it becomes favourable to propagate laterally. We

estimate the total strain energy before and after advance of a dyke segment by

numerically integrating the strain energy density over a large volume,

$$(2) \qquad\qquad \Theta_s = \frac{1}{2} \int \sigma_{ij} \varepsilon_{ij} dV$$

where σ_{ij}, ε_{ij} and dV are the components of stress tensor, strain tensor, and the volume element of integration[15]. We approximate the change in gravitational energy in surrounding crust, for each dyke segment, by integrating the predicted vertical displacements, multiplied by the local topographic load density (ice and crust) above a reference surface, and the acceleration of gravity (Methods). Dyke formation is associated with uplift on their flanks; the lower the topographic load over the flanks, the less energy it costs. For any given location on a volcano, the strike of a new dyke segment will influence the strain and gravitational potential energy change in a different way. The direction that minimizes the combined energy should be favoured (Methods and Extended Data items 7-8). For the Bárðarbunga 2014 rifting event the actual propagation path closely follows that predicted by our model (Fig. 3b), and can in particular explain why the dyke propagation changed to a northerly direction after initially propagating to the southeast. The influence of topography is large during the first segments but decreases as the dyke propagates towards more level topography and the tectonic stress becomes dominant in determining the direction of the dyke propagation; in essence the dyke is captured by the plate spreading field once it is sufficiently far from the Bárðarbunga central volcano, which is located to the west of the central axis of the plate spreading model invoked (Methods). We have assumed in our model that the dyke remains at a fixed depth with respect to sea level, as it propagates. If in fact the dyke maintains a level of neutral buoyancy, the influence of topography will be about one third greater (Methods), changing the predicted path slightly.

Our results show the dyke is heterogeneous in terms of seismic moment release and vertically integrated magma volume, peaking on the segments where the dyke halted, at 20-28 km and 33-39 km along the dyke (Fig. 2a). These are also locations where magma possibly reached the surface as revealed by the ice cauldrons formed (Fig. 2b). The longest halt in the dyke propagation on 19-23 August correlates with increased lithostatic pressure, for any given depth, in the direction of propagation, (Extended Data item 8). Lateral dyke propagation is facilitated if a dyke advances into an area with falling lithostatic pressure, as the level of neutral buoyancy drops[18]. Such a process can be driven by gravity alone, but farther propagation when the lithostatic pressure increases requires the dyke to propagate upwards. Several days of magma flow to the Bárðarbunga dyke tip were required to increase the internal pressure sufficiently and drive propagation past the largest barrier along its path. Our seismic and geodetic observations provide details of a lateral dyke advance in segments, which can be related to the effects of the plate boundary stress field and topography on dyke steering and segmentation, with flow influenced by along-dyke variation in the lithostatic pressure profile. Similar studies, that may in future be carried out in near real-time, can lead to improved understanding of the evolution and forecasting of the behaviour of lateral dykes in various tectonic settings[19,20].

References

1. Wright, T. J. *et al*. Geophysical constraints on the dynamics of spreading centres from rifting episodes on land. *Nature Geoscience* **5**, 242–250, doi:10.1038/ngeo1428 (2012).

2. Einarsson, P. & Brandsdottir, B. Seismological evidence for lateral magma intrusion during the July 1978 deflation of the Krafla volcano in NE-Iceland. *J. Geophys.* **47**, 160–165 (1980).

3. Buck, W. R., Einarsson, P. & Brandsdottir, B. Tectonic stress and magma chamber size as controls on dike propagation: Constraints from the 1975–1984 Krafla rifting episode. *J. Geophys. Res.*, **111**, B12404, doi:10.1029/2005JB003879 (2006).

4. Belachew, M. *et al.* Comparison of dike intrusions in an incipient seafloor-spreading segment in Afar, Ethiopia: Seismicity perspectives, *J. Geophys. Res.*, **116** (B6), B06405, doi:10.1029/2010JB007908 (2011).

5. Gudmundsson, A. Infrastructure and mechanics of volcanic systems in Iceland. *J. Volcanol. Geotherm. Res.* **64**, 1–22 (1995).

6. Hartley, M. E. & Thordarson, T. The 1874–1876 volcano-tectonic episode at Askja, North Iceland: Lateral flow revisited. *Geochem. Geophys. Geosyst.* **14**, 2286–2309, doi:10.1002/ggge.20151 (2013).

7. Segall, P. *Earthquake and Volcano Deformation*, Princeton University Press (2009).

8. Segall, P., Llenos, A. L., Yun, S.-H. Bradley, A. M., & Syracuse, E. M. Time-dependent dike propagation from joint inversion of seismicity and deformation data. *J. Geophys. Res. Solid Earth* **118**, doi:10.1002/2013JB010251 (2013).

9. Björnsson, H. *Hydrology of ice caps in volcanic regions*, Societas scientarium Islandica, rit 45, 139 pp, 21 maps. Reykjavik (1988).

10. Gudmundsson, M.T. & Högnadóttir, T. Volcanic systems and calderas in the Vatnajökull region, central Iceland, constraints on crustal structure from gravity data. *Journal of Geodynamics* **43**, 153-169 (2007).

11. Björnsson, H. & Einarsson, P. Volcanoes beneath Vatnajökull, Iceland: Evidence from radio-echo sounding, earthquakes and jökulhlaups, *Jökull* **40**, 147-168, 1990.

12. Thordarson, T. & Larsen G. Volcanism in Iceland in historical time: Volcano types, eruption styles and eruptive history. *Journal of Geodynamics* **43**, 118-152, (2007).

13. Einarsson, P. *et al*. Center of the Iceland hotspot experiences volcanic unrest. *EOS, Transaction of the American Geophysical Union* **70**, 369-375 (1997).

14. Pagli, C. *et al*. Crustal deformation associated with the 1996 Gjálp subglacial eruption, Iceland: InSAR studies in affected areas adjacent to the Vatnajökull ice cap. *Earth and Planetary Science Letters* **259**, 24-33 (2007).

15. Reddy, J. N. *An Introduction to Continuum Mechanics*, Cambridge University Press (2013).

16. Dahm, T. Numerical simulations of the propagation path and arrest of fluid-filled fractures in the Earth, *Geophysical Journal International* **141**, 623-638 (2000).

17. Maccaferri, F., Bonafede, M. & Rivalta, E. A quantitative study of the

mechanisms governing dike propagation, dike arrest and sill formation, *Journal of Volcanology and Geothermal Research* **208,** 39–50 (2011).

18. Fialko, Y.A. & Rubin, A. What controls the along-strike slopes of volcanic rift zones? *J. Geophys. Res.* **104**, 20007-20020 (1999).

19. Toda, S., Stein, R. S. & Sagiya, T. Evidence from the AD 2000 Izu islands earthquake swarm that stressing rate governs seismicity. *Nature* **419**, 58-61 (2002).

20. Staudacher, T. *et al*. The April 2007 eruption and the Dolomieu crater collapse, two major events at Piton de la Fournaise (La Réunion Island, Indian Ocean). *J. Volc. Geotherm. Res.*, **184**,126–137 (2009).

Authors contributions

The writing of the paper, and the research it is based on, was coordinated by the first five authors and other members of Icelandic Meteorological Office (IMO) seismic monitoring team. All authors contributed ideas and input to the research and writing of the paper. Modeling of geodetic data was done by A.H., E.R.H. and Th.A. Analysis and operation of continuous GPS sites were carried out by S.H., B.Ó., H.M.F, R.B., V.D., H.G., and P.L. Relative earthquake locations were done by K.S.V., seismic data presentation and relative locations by G.B.G., focal mechanisms by M.H. and single earthquake locations led by K.J. and SIL seismic monitoring

14

group. Interferometric analysis was carried by S.D., K.S., M.P., V.D., S.S., with a composite digital elevation model prepared by E.M. The combined strain and gravity potential in relation to the dyke propagation was modelled by E.R.H. in consultation with A.H. and F.S. Campaign GPS measurements were carried out by S.D., V. D., M.P., A.R.H., E.S., F.S., and others. M.T.G. and Th.H. mapped the collapse of the Bárðarbunga caldera and the formation of ice cauldrons over the path of the dyke with aircraft radar profiling. A.R.H, E.M. and P.E. led mapping of graben formed and eruptive fissure as shown here. P.E., B.B., and R.P. contributed to the interpretation of events, and H.B. and F.P. provided bedrock topography and ice thickness for Vatnajökull ice cap. R.S.W., T.A., T.G., R.G.G., C.J.B, M.M., A.B., and E.P.S.E. contributed and analysed seismic data.

Main figure legends (522 words / max total 500 words)

Figure 1. Overview of data. **a**, Earthquakes 16/08-06/09 2014 (dots) and horizontal ground displacements measured by GPS (arrows) on a map with central volcanoes (oval outlines), calderas (hatched), and northern Vatnajökull. Relatively relocated epicentres and displacements are colour coded according to time of occurrence, other single earthquake locations are in grey. Rectangles show areas displayed in Fig. 2; thin lines within them show inferred dyke segments. The red shading at Bárðarbunga caldera shows subsidence up to 16 m inferred from radar profiling on 5 September. The star marks the location of the magma source inferred from modelling. Also shown are ice cauldrons formed (circles), outline of lava flow mapped from radar image on 6 September, and eruptive fissures (white). **b**, Wrapped RADARSAT-2

interferogram spanning 08/08-01/09 2014. Shading at Bárðarbunga caldera shows unwrapped one day (27-28/08) COSMO-SkyMed interferogram with maximum LOS increase of 57 cm. Also shown are earthquakes (grey dots), boundaries of graben activated in the dyke distal area (hatched lines), and location of interferograms in panels c and d (boxes) **c**, Unwrapped Cosmo-SkyMed interferogram spanning 13-29 August. **d**, Unwrapped TerraSAR-X interferogram spanning 26/07-4/09 2014. Satellite flight and viewing direction are shown with black and white arrows, respectively. LOS displacement is positive away from the satellite for all interferograms shown.

Figure 2. Seismicity and magma volume along the dyke, 16/08-6/09 2014. Relocated earthquakes shown in Fig. 1 are indicated, with same colour coding. **a**, Daily cumulative seismic moment at 0.5 km intervals along the dyke. **b**, Plan-view of four rotated areas along the dyke. Arrows indicate geographic north. Dots denote epicentres, black lines dyke segments, and open circles ice cauldrons. Fault-plane solutions for selected earthquakes are shown. **c**, Earthquake depths referenced to sea level. **d**, Daily vertically integrated volume of magma along the dyke inferred from geodetic modelling.

Figure 3. Dyke model. **a**, Median of the posterior probability of opening for dyke patches inferred from modelling, and relocated earthquake hypocentres (black dots) relative to sea level. Red stars mark the eruption sites. **b**, Preferred direction of dyking for different segments based on a model of combined strain and gravitational potential energy release. Blue lines represent dyke segments and grey dots earthquake epicentres. Black dots indicate the beginning of each segment and surrounding

16

coloured points represent possible end points for different strikes of propagation. Their colour indicates $(E - E_{min})/(E_{max} - E_{min})$ where E is the energy state for a particular strike, and E_{min} and E_{max} are the minimum and maximum energy state for that segment. Background shows bedrock topography.

Figure 4. Seismicity along the length of the dyke as a function of time (left y-axis) and volume change of the dyke (blue) and magma source (red) (right y-axis). The volumes (with 95% confidence intervals) are estimated from available geodetic data for each day using a model of a point pressure source and two dip-slip faults beneath the caldera. The magma source volumes are scaled by a factor of two, such that the value estimated for 5 September from GPS and InSAR data alone becomes equal to that estimated when the caldera subsidence is added to the inversion. Shading indicates the Holuhraun eruptions.

Methods (2690 words**)**

Seismic analysis. Seismicity was recorded by the Icelandic national, SIL, seismic network complemented with seismometer installations from University of Cambridge, and University College Dublin. Events attributed to the laterally growing dyke are volcano tectonic events. Initial single earthquake locations are performed by minimising the square sum of both P- and S-wave arrival time residuals in the SIL analysis software[21]. Relative relocations are obtained by iterative inversion of the

weighted square sums of: absolute P- and S arrival time differences, as well as the double differences of (i) absolute arrival times of P- and S-waves, (ii) relative arrival times of P- and S-waves and (iii) relative S-P arrival times[22]. Each event is inverted in a group with of over 40 of its nearest neighbours. Overlap of groups is enough to ensure that most events are located in at least 5 groups. The solutions shown are obtained using the SIL velocity model which is the standard one dimensional (1D) reference velocity model of the SIL analysis system[23]. In the relative earthquake locations the different elevations of seismic stations are not taken into consideration, except through the relative importance of the stations in the inversion for best locations (i.e the number of phases used). The average elevation of the dominant stations (0.9 km) is therefore taken as the initial reference elevation of the relative location results. To reference the location results to sea level, the depths were therefore shifted upwards by 0.9 km. To estimate the dependence of the location results on velocity model, the relative locations were also calculated in a second velocity model (IMO-vj), which is a rough 1D approximation to the velocity on the ICEMELT refraction profile at the northern margin of Bárdarbunga[24]. This model gives source depths which are within 100 m in lateral distance but mostly around 2.5 km deeper than in the SIL model. This is likely caused by the lower velocities in the IMO-vj model below 6 km depth (Supplementary Fig. 7). Even though relative earthquake location errors can be quite small, there is always ambiguity about absolute location accuracies. The location of the ice depressions above the dyke segments where the dyke propagation temporarily stalled, and the location of the graben subsidence directly above the seismicity confirms the quality of the absolute lateral locations. To further test the absolute depth accuracies, one hundred events along the whole dyke were selected and located with NonLinLoc[25] in another

approximation to the ICEMELT profile at Vatnajökull (CAM-vatnaj). The results, referenced to sea level (Supplementary Figs. 7 and 8), show a very similar depth range to the relative locations and further support the absolute vertical location quality of the earthquakes. The two models, SIL and CAM-vatnaj, have a very different shallow structure, but below 6.5 km, where most of the seismicity is concentrated, they are very similar.

Focal mechanisms (Fig. 2) are best fitting solutions using a lower hemisphere projection based on grid search over all strike, dip and rake combinations matching observed P-wave polarities and within allowed limits from observed spectral amplitudes of P- and S-waves[26]. Exemplary mechanisms of earthquakes M>2 and at least six fitting P-wave polarities have been selected for each subcluster of the dyke intrusion. Focal mechanisms have tensional axes consistently orientated near perpendicular to the dyke as expected near dykes[19], while pressure axes are variable depending on the location of the event w.r.t. the dyke (i.e., above or in front of it).

GPS analysis. Significant deformation was observed at 16 pre-existing CGPS stations in relation to the Bárðarbunga events in 2014. Five additional sites were installed during the unrest leading up to the Holuhraun fissure eruption, all installed next to or on existing monuments (Supplementary Table 1). Additional sixteen sites were measured regularly during the unrest (Supplementary Table 2). Multiple measurements were made at all these sites prior to the Bárðarbunga unrest, with the exception of the site GSIG, which was installed and first measured in June 2014. GSIG is located about 700 meters from an existing benchmark. The last GPS campaign in the region was conducted from 28 July to 9 August 2014.

The GPS data were analysed using the GAMIT/GLOBK software, version 10.4 (ref. 27), using over 100 global reference stations. Average site positions were evaluated in the ITRF08 reference frame every 24 hour UTC day. The continuous GPS data were furthermore divided into three eight hour sessions with a running 24 hour window of reference station and orbit data, to provide higher temporal resolution (Supplementary Fig. 1a-f). In addition to station coordinates, the processing solved for satellite orbit and earth rotation parameters, atmospheric zenith delay every two hours, and three atmospheric gradients per day. Ocean loading was corrected for using the FES2004 model. The IGS08 azimuth and elevation dependent absolute phase centre model was applied for all antennas. Pre-rifting site velocities were estimated based on all existing data and removed from the data. The last three to six days of measurements at each site prior to August 16 were then used to estimate a reference epoch. Data affected by snow and ice were removed during the analysis.

Interferometric analysis of X-band satellite data (wavelength ~3.1 cm) from the COSMO-SkyMed and TerraSAR-X satellites was undertaken using the Repeat Orbit Interferometry Package (ROI_PAC)[28] and DORIS software[29]. Analysis of C-band RADARSAT-2 data (wavelength ~5.56 cm) was computed using the GAMMA software[30]. Topographic signal in the interferograms was estimated using a LiDAR DEM[31] on the glacier and for an area extending 2-3 km from the glacier margin. Further from the glacier an intermediate DEM from the TanDEM-X mission was used with a DEM from the ASTER satellite mission and the EMISAR DEM[32] to fill in observed gaps. The DEM mosaic used for the topographic correction has pixel size of 30 m (the pixel size of the ASTER DEM). Interferograms were filtered using a power spectrum filter[33] and unwrapped using the branch cut algorithm[34] and the snaphu minimum-cost-flow method[35]. We downsampled all interferograms using an adaptive

quadtree approach[36], with a cut-off variance of 10^{-3} m^2. Interferograms are shown in Supplementary Fig. 2 and a list of all interferograms used is in Supplementary Table 3.

The subsiding graben was mapped from high resolution radar images from the airborne radar system on-board the Icelandic Coast Guard aircraft TF-SIF, and photographs taken on-board the same airplane. The photographs were also used to obtain coordinates for the eruptive fissures. The photographs were geo-referenced by comparison with older geo-referenced aerial photographs from Loftmyndir Corp., using the ArcGIS software. The radar images were geo-referenced with the LiDAR DEM[30] using MATLAB®R2013a and Surfer 12 (©Golden Software, Inc.).

Deformation Modelling. Measurement errors were assumed to be drawn from a zero-mean Gaussian distribution and errors in the physical model were assumed to scale up the effective measurement error. Application of Bayes' theorem gives the *a posteriori* probability distribution for the model parameters as

$$p(\mathbf{m}, \sigma, |\mathbf{d}) = K\sigma^{-N} \exp\left\{-\frac{1}{2\sigma^2}(\mathbf{d} - \mathbf{Gm})^T \Sigma_{\mathbf{d}}^{-1}(\mathbf{d} - \mathbf{Gm})\right\} p(\mathbf{m}),$$

where $\mathbf{m}$ is the vector of model parameters, $\mathbf{d}$ is the vector of measurements, $\mathbf{G}$ is a matrix of Green's functions mapping slip to displacements, $\Sigma_{\mathbf{d}}$ is the variance-covariance matrix for the measurements, σ^2 is the scaling factor due to model error, N is the number of measurements, K is a normalising constant and $p(\mathbf{m})$ is the *a priori* probability of the model parameters. The covariance of the error for each pair of InSAR measurements is calculated assuming a one dimensional exponential

covariance function: $Cov = 0.0016\exp(-h/5)$ m^2, where h is the distance between the measurement points in km. The model parameters are opening and strike-slip for the dyke patches[37], position and pressure decrease of a penny-shaped crack[38] or point pressure source[39], a bilinear orbital error ramp for each interferogram, and the hyperparameter σ^2. We allow for slip as well as opening, as dykes that are not perpendicular to the minimum compressive stress direction will be subject to shearing across the dyke walls[40]. We set the *a priori* probability to allow only positive opening and slip in the direction consistent with the regional stress field from relative plate motions. During the geodetic modelling the different elevation of geodetic stations was not taken into consideration. The initially inferred depths were therefore shifted by the average elevation of the GPS stations (1.0 km), resulting in geodetic model depths relative to sea level (shown here).

The *a posteriori* distribution is sampled using a Markov chain Monte Carlo algorithm, incorporating the Metropolis algorithm[41]. This involves selecting an initial value for each of the model parameters from $p(\mathbf{m})$ and calculating the likelihood function, which is the right hand side of the equation above excluding $p(\mathbf{m})$. A trial random step is then taken within $p(\mathbf{m})$, and the new likelihood value is calculated. If the new likelihood value is greater, the step is taken and the trial model values are retained. If less, there is a chance that the step is taken, which is calculated as the ratio of the new likelihood over the old likelihood. Otherwise the old model values are retained. A new trial random step is taken, and the process is repeated until a representative sampling of the whole *a posteriori* distribution is built. The efficiency of this algorithm in reaching this goal depends on the maximum size of the random step that may be taken within $p(\mathbf{m})$. In order to ensure fast convergence, we perform a sensitivity test for each model parameter after every 1000 iterations, and adjust the

maximum step size such that all parameters contribute approximately equally to the change in likelihood and, as a whole, the mean chance of acceptance is approximately 50% (ref. 42).

The models of the deflation at Bárðarbunga are more uncertain than the dyke; however, whichever model we choose for the deflation, the modelled values of dyke opening do not change significantly.

Strain potential energy change associated with dyke formation require an estimate of tectonic stress (deviatoric stress induced by plate movements). To estimate strain potential we assumed that the tectonic stress due to plate spreading could be estimated by an infinitely long and wide tensile dislocation below 10 km depth in an elastic half-space. Such a kinematic model has been used successfully to fit GPS observations across the plate boundary in Iceland[43]. This tensile dislocation was opened 4 m, which would correspond to stress built up by plate spreading for more than 200 years. It was located so that it would be under the Askja central volcano as geodetic measurements have indicated that the central axis of plate spreading pass through there[44]. The strike of this dislocation was set to N12°E, to be about perpendicular to direction of plate movements predicted by global plate motion models. We assume the tectonic stress throughout the depth interval of the crust considered does not vary with depth, similarly to the approach of Buck *et al.*[3]. The value of stress we use is that calculated at 10 m depth in the dislocation model. We calculate the stress and strain due to a dyke segment opening in a similar manner and superpose them on the estimated tectonic contributions. Assuming a linear relationship between stress and strain, we then calculate the strain energy potential using equation (2).

Gravitational potential energy change is here calculated, for each dyke segment, as described in the text by integrating the predicted vertical displacements associated with the dyking, multiplied by the local topographic load density (ice and crust) above an arbitrary reference surface (taken here as sea level), and the acceleration of gravity. Two digital elevation models are used, one of which covers the surface of the Vatnajökull icecap and extends beyond the limits of the icecap, and the other which represents the ice thickness. The map of the sub-ice topography was compiled from continuous ice thickness profiling by radio echo-sounding along a series of traverses over the ice cap[9,11]. Along the complete length of the dyke the change in lithostatic pressure corresponds to an effective crustal load change of about 900 m (Extended Data item 8). However, variations in the effective load in areas adjacent to an individual dyke segment influenced by vertical displacements are much smaller, typically on the order of several hundred meters or less. This is an order of magnitude less than the 2 km depth to the top of a "test dyke segment" used for calculation of the preferred path of dyking (see below). Thus, we can consider small perturbations to the vertical deformation field introduced by the real topography to be second order.

When inferring the path of preferred dyke propagation, we assume also that the dyke depth, with respect to sea level, is the same for all strikes tested. In reality the dyke may track the level of neutral buoyancy, resulting in the preferred depth of dyking varying with strike. In our approach, the dyke moving down by one metre (with respect to sea level) can be considered equivalent to increasing the load on the reference surface by one metre of crust. The associated increase in potential energy change (compared to that when the dike stays at the same depth) will be equal to the integrated vertical displacement of the reference surface multiplied by the density of

the crust and gravitational acceleration. On the other hand, the reduction in potential

energy from lowering the magma will be equal to the volume of the dyke multiplied

by the density of the magma and gravitational acceleration. For a Poisson's ratio of

0.25, the integrated surface uplift is 75% of the dyke volume[48]. Therefore ~25% less

energy is needed to lift the extra crust than is released by lowering the dyke, i.e., the

energy released in lowering the dyke is ~33% more than needed to lift the extra crust.

This means that if the dyke propagates at a level of neutral buoyancy, rather than

remaining at a fixed depth (with respect to sea level), the differences in gravitational

potential energy change with strike will be ~33% larger than we calculate, thus

increasing the influence of topography still further.

Calculation of the preferred path of dyking. For combined potential energy

change during dyking, we here estimate all parameters based on seismic and geodetic

data except the strike of a dyke segment. Each segment, whose location and length are

determined from relative earthquake locations, is assumed to be a rectangular tensile

dislocation[36]. The depth to the top of each dislocation is fixed to 2 km for all

segments, the width (height) is fixed to 4 km and opening is fixed to 3 m. The starting

point of each segment is fixed adjacent to the previous segment (blacks dot on Fig.

3b). This assures that only energy states which assume continuation of the magma

flow are considered. Then the strike of the segment is varied so that it is rotated

around its starting point. The strike is varied well over 180 degrees in search of the

minimum energy for emplacement of the new segment. To implement the approach

we performed two integrations, one in three dimensions for the strain potential energy

and one in two dimensions for the gravitational potential energy. A Monte Carlo

numerical integration in MATLAB was used, where a mean value was estimated and multiplied by the volume, for strain energy, or area, for gravitational energy. The rectangular dislocation formula does not take into account the strength of the material and in its vicinity the strain energy density is non-realistic and close to singular values. To avoid these values we assigned zero to energy density values over three orders of magnitude larger than the estimated average value. Therefore we did not evaluate the strain energy densities in the immediate vicinity of a dyke intrusion, but rather evaluated how tectonically stressed crust will respond to dyke opening and if that opening will increase or decrease the total potential energy of the crust. The area of integration included a radius greater than 50 km from each dyke segment. The strain energy density was integrated down to a depth of 20 km. We found this was sufficient so that the boundaries did not influence the estimated energy changes. To calculate the stress and strain tensors as well as the vertical surface displacements we used disloc3d, software developed by the Crustal Deformation and Fault Mechanics research group at Stanford University.

Additional references

21. Böðvarsson, R., Rögnvaldsson, S.T., Slunga, R. & E. Kjartansson, E. The SIL data acquisition system - at present and beyond year 2000, Icelandic Meteorological Office, report VÍ-R98005-JA04 (1998).

22. Slunga, R., Rögnvaldsson, S.Th. & Bödvarsson, R. Absolute and relative locations of similar events with application to microearthquakes in southern Iceland. *Geophys. J.Int.* **123**, 409-419 (1995).

23. Stefánsson, R. *et al*. Earthquake prediction research in the South Iceland seismic zone and the SIL project. *Bull. Seismol. Soc. Am.* **83**, 696-716 (1993).

24. Darbyshire, F. A., Bjarnason, I. Th., White, R. S. & Flóvenz, Ó. G. Crustal structure above the Iceland mantle plume imaged by the ICEMELT refraction profile. *Geophysical Journal International,* **135**, 1131–1149 (1998).

25. Lomax, A., J. Virieux, J., Volant, P. & Berge, C. Probabilistic earthquake location in 3D and layered models: Introduction of a Metropolis-Gibbs method and comparison with linear locations, in *Advances in Seismic Event Location*, Thurber, C.H., & Rabinowitz, N. (eds.), Kluwer, Amsterdam, 101-134 (2000).

26. Rögnvaldsson, S.T. & R. Slunga, R. Routine fault plane solutions for local networks: A test with synthetic data, *Bull. Seism. Soc. Am*. **83**, 1232–1247 (1993).

27. Herring, T., King, R. W. & McCluskey S. M. *Introduction to GAMIT/GLOBK release 10.4*, Mass. Inst. of Technol. Technical Report, Cambridge (2010).

28. Rosen, P.A., Henley, S., Peltzer, G. & Simons, M. Updated repeat orbit interferometry package released. *EOS Trans Am Geophys Union* **85**(5):47 (2004).

29. Kampes. B. Delft Object-oriented Radar Interferometric Software: User's manual and technical documentation, v4.02 edition (1999).

30. Wegmuller, U. & Werner, C. *Gamma SAR processor and interferometry software*. In The 3rd ERS symposium on space at the service of our environment, Florence, Italy, 1997.

31. Jóhannesson, T. *et al*. Ice-volume changes, bias-estimation of mass-balance measurements and changes in subglacial water bodies derived by LiDAR-mapping of the surface of Icelandic glaciers. *Annals of Glaciology* **54**(63), 63-74 (2013).

32. Magnússon, E., Björnsson, H., Dall, J. & Pálsson, F. Volume changes of Vatnajökull ice cap, Iceland, due to surface mass balance, ice flow, and subglacial melting at geothermal areas. *Geophysical Research Letters* **32**, L05504 (2005).

33. R. Goldstein, R. & Werner, C. Radar interferogram filtering for geophysical applications. *Geophysical Research Letters* **25**(21), 4035-4038 (1998).

34. Goldstein, R., Zebker, H. & Werner C. Satellite radar interferometry-two-dimensional phase unwrapping. *Radio Science* **23** (4), 713–720 (1988).

35. Chen, C. W., & Zebker, H. A. Two-dimensional phase unwrapping with use of statistical models for cost functions in nonlinear optimization. *JOSA A* **18**(2), 338-351 (2001).

36. Decriem, J. *et al*. The 2008 May 29 earthquake doublet in SW Iceland. *Geophysical Journal International* **181**(2), 1128-1146 (2010).

37. Okada, Y. (1992). Internal deformation due to shear and tensile faults in a half-space. *Bulletin of the Seismological Society of America* **82**(2), 1018-1040 (1992).

38. Fialko, Y., Khazan, Y., & Simons, M. Deformation due to a pressurized horizontal circular crack in an elastic half-space, with applications to volcano geodesy. *Geophysical Journal International* **146**(1), 181-190 (2001).

39. Mogi, K. Relations between the eruptions of various volcanoes and the deformations of the ground surfaces around them, *Bull. Earthquake Res. Inst. Univ. Tokyo* **36**, 99-134 (1958).

40. Hooper, A. *et al*. Increased capture of magma in the crust promoted by ice-cap retreat in Iceland. *Nature Geoscience* **4**, 783-786, doi:10.1038/ngeo1269 (2013).

41. Mosegaard, K. & Tarantola, A. Monte Carlo sampling of solutions to inverse problems. *J. Geophys. Res.* **100**, 12,431–12,447 (1995).

42. Hooper, A. *et al*. Importance of horizontal seafloor motion on tsunami height for the 2011 M_w=9.0 Tohoku-Oki earthquake. *Earth and Planetary Science Letters* **361**, 469-479 (2013).

43. Árnadóttir, T., Jiang, W. Feigl, K. L. Geirsson, H. & Sturkell, E. Kinematic models of plate boundary deformation in southwest Iceland derived from GPS observations. *J. Geophys. Res.* **111**, B07402 (2006).

44. Sturkell, E. & Sigmundsson, F. Continuous deflation of the Askja caldera Iceland,

during the 1983-1998 non-eruptive period. *J. Geophys. Res*. **105**, 25671-25684

(2000).

45. Jóhannesson, H. & Sæmundsson, K. *Geological Map of Iceland*, *Tectonics*,

1:600.000, Icelandic Institute of Natural History (2009).

46. Gudmundsson, M.T., Högnadóttir, Þ., Kristinsson, A.B. & Gudbjörnsson, S.

Geothermal activity in the subglacial Katla caldera, Iceland, 1999-2005, studied with

radar altimetry. *Annals of Glaciology* **45**, 66-72 (2007).

47. Yun, S., Segall, P. & Zebker, H. Constraints on magma chamber geometry at

Sierra Negra Volcano, Galápagos Islands, based on InSAR observations. *Journal of

Volcanology and Geothermal Research* **150**. 232-243 (2006).

48. Delaney, P. T & McTigue, D. F. Volume of magma accumulation or withdrawal

estimated from surface uplift or subsidence, with application to the 1960 collapse of

Kilauea volcano. *Bull. Volcanol*. **56**, 417-424 (1994).

Legends to Extended Data items

Extended Data item 1. Tectonic map showing seismic and geodetic stations. Filled

triangles correspond to continuous GPS stations, open triangles to campaign GPS

sites, and filled inverted triangles to seismic stations. Station names for GPS are

indicated with four capital characters and for seismic stations with three lower case

letters. The different tracks for SAR satellite data are plotted with straight lines for RADARSAT-2, dashed lines for COSMO-SkyMed (CSK), and dotted lines for TerraSAR-X (TSX). Their orbit numbers are also indicated. The stars correspond to the eruptive fissures at Holuhraun. Background map shows ice caps (white), central volcanoes (dotted lines), calderas (hatched lines), and fissure swarms (gray shading)[45]. Names of selected volcanoes shown, T for Tungnafellsjökull central volcano. The inset box shows the Eastern Volcanic Zone (EVZ), the Western Volcanic Zone (WVZ), the Northern Volcanic Zone (NVZ), the South Iceland Seismic Zone (SISZ), with their fissure swarms and central volcanoes. The rectangular box within the inset shows the area of the main image.

Extended Data item 2. Map and table of dyke segments defined by seismicity.
a) Location of dyke segments delineated by relatively relocated earthquakes. The triangles show locations of the nearest seismic stations used to locate the events. Green stations operated by the Icelandic Meteorological Office (IMO), blue station operated by the University of Cambridge, and red station operated by University College Dublin. All stations telemetered data to IMO. The two stations on the ice are IMO stations installed under the FUTUREVOLC project, temporarily operating with sensors from the University of Cambridge, on loan from Seis UK. Also shown are ice cauldrons formed (circles), outline of lava flow mapped from radar image on 6 September, and boundaries of graben activated in the dyke distal area (hatched lines).
b) The dyke segments. Columns show segment number (Nr), latitude and longitude of beginning (Lat1, Long1) and end points (Lat2, Long2) of each segment, segment length (L), depth range (D), strike, dip, the RMS value of the deviation (in meters) of

the earthquakes from the plane they define, and the number of earthquakes used to define each dyke segment plane (#Eq).

Extended Data item 3. Subsidence at Bárðarbunga volcano revealed by airplane radar profiling. The blue contours show the elevation of the ice surface in the Bárðarbunga caldera on 5 September 2014, about three weeks after the onset of unrest. The data are obtained using aircraft flown 100-150 meters above glacier surface, using radar altimetry and submeter differential GPS Omnistar. The system provides 2 m absolute accuracy of surface elevation along the survey profiles[46], shown as black dotted lines. The subsidence relative to the pre-unrest ice surface is indicated with the red shading. It is greatest in the central part of the caldera where it had a maximum of 16 m.

Extended Data item 4. Geodetic model with a two-segment-dyke and no *a priori* constraints. Maximum probability solution for a model with a contracting point pressure source[37] and a dyke modelled as two segments with uniform opening[39]. Position and volume change of the point source and position, strike, dip and opening of the dyke are free parameters. The panels show from left to right: data (a, d, g), model (b, e, h) and residuals (c, f, i). GPS data in all panels span 15 August to 4 September 2014. The top panels (a-c) show an interferogram spanning 6 July 2012 to 4 September 2014. The middle panels show an interferogram spanning 2 August to 3 September 2014 (d-f). The bottom panels show the data from Extended Data item 3 from airplane radar profiling (g-i).

Extended Data item 5. Geodetic model with a point pressure source, caldera faults, and a four-segment-dyke. Maximum probability solution for a model with a contracting point pressure source[37], two dip-slip faults beneath the caldera, and a dyke modelled as four segments divided into multiple rectangular patches[39]. Lateral dyke position is fixed from relocated seismicity. Position of the point source and faults, volume change of the point source and opening and strike-slip of the dyke are free parameters. The data used are detailed Extended Data item 4.

Extended Data item 6. Geodetic model with a flat-topped chamber, caldera faults, and a four-segment-dyke. Maximum probability model with a deflating penny-shaped crack[38] (used to represent the top of a flat topped chamber[47]), two dip-slip faults beneath the caldera, and a dyke modelled as four segments divided into multiple rectangular patches[39]. Lateral dyke position is fixed from relocated seismicity. Position of the crack and faults, volume change and radius of the crack and opening and strike-slip of the dyke are free parameters. The data used are detailed in Extended Data item 4.

Extended Data item 7. Path of dyke propagation from energy considerations. Energy profiles (a-h) for the segments 1-8, respectively as described in Fig. 3b. Blue lines indicate the strain energy potential change as a function of the strike, and the red lines the gravitational potential change. Green is the total potential energy change. Energy is shown in TeraJoules (10^{12} J). The lowest point on each energy curve is defined as 0 TJ. Error bars represent one standard deviation of the error in the numerical integration.

Extended Data item 8: Topography, earthquake depths, and lithostatic pressure along the dyke path. a, Bedrock and ice topography along the dyke path. **b,** Depth of earthquake hypocentres below sea level projected on the dyke segments and lines (red) of constant lithostatic pressure, assuming constant crustal density of 2800 kg/m^3 and ice density 920 kg/m^3. Line spacing corresponds to 25 MPa. **c,** Lithostatic pressure at sea level calculated along dyke segments 1, 2, 3, 4, 5, 6, 7a, 8a and 8b. The calculations take into account both the sub-glacial bedrock topography and the ice thickness. Light blue triangles indicate the beginning of a segment and red triangles the end of a segment. It's assumed that between segments the dyke propagates along a straight path. Dyke propagation was halted for the longest time at the end of segment 4 (see Figs. 2 and 4 in main text), prior to increase in lithostatic pressure.
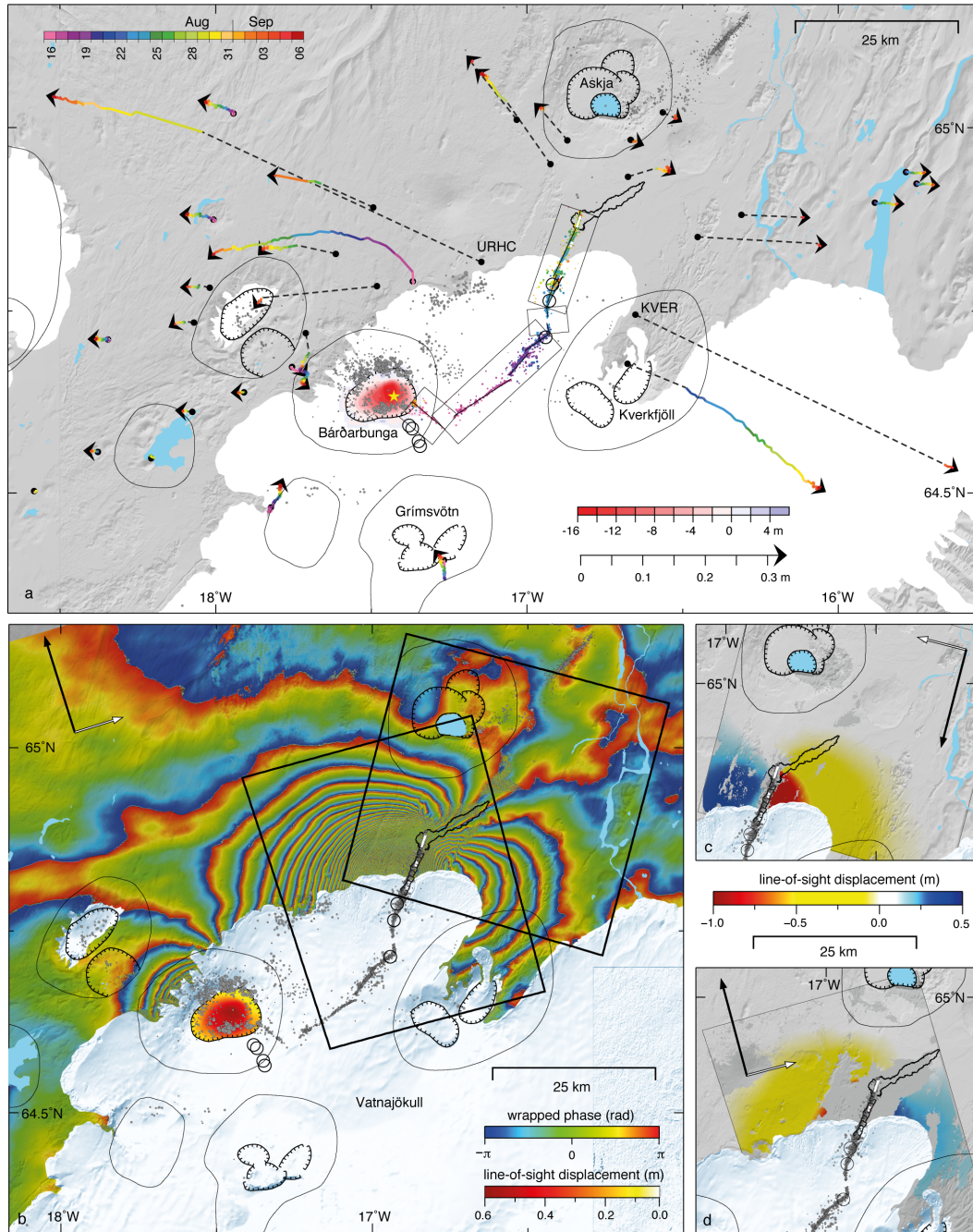
Fig. 1
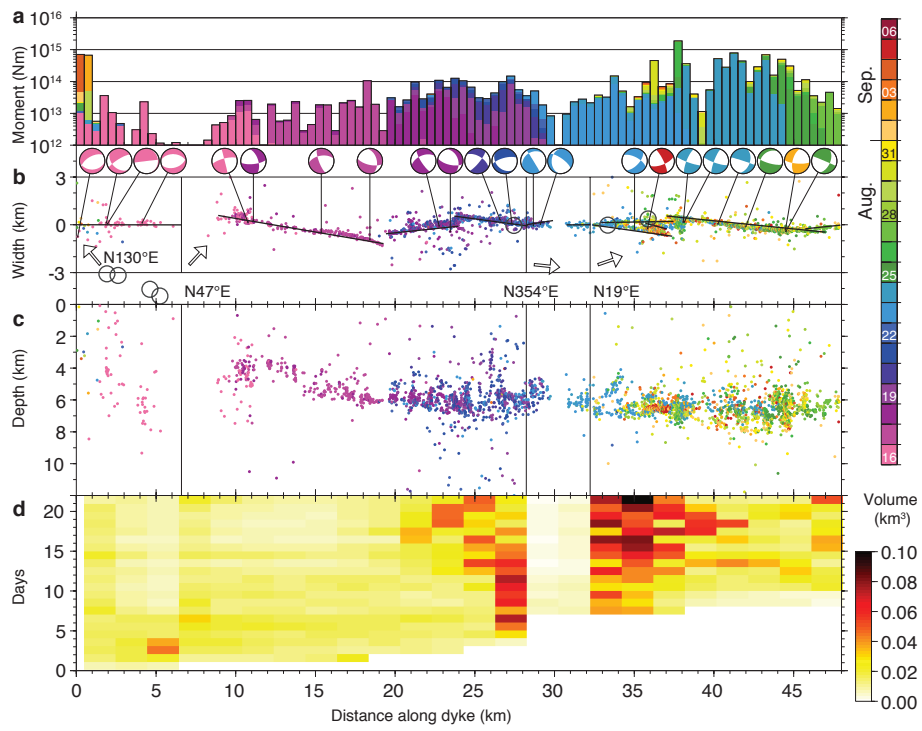
Fig. 2
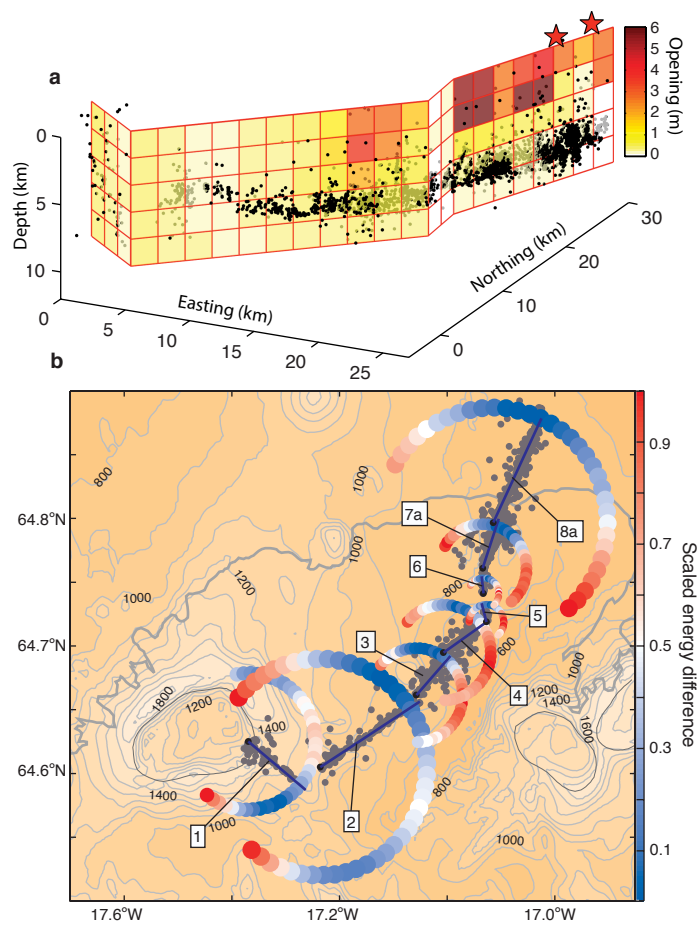
Fig. 3
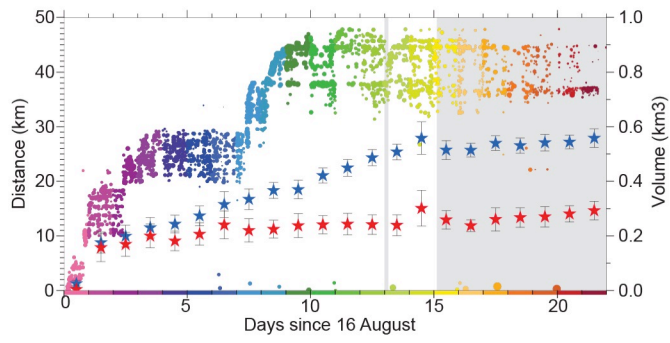
Fig. 4
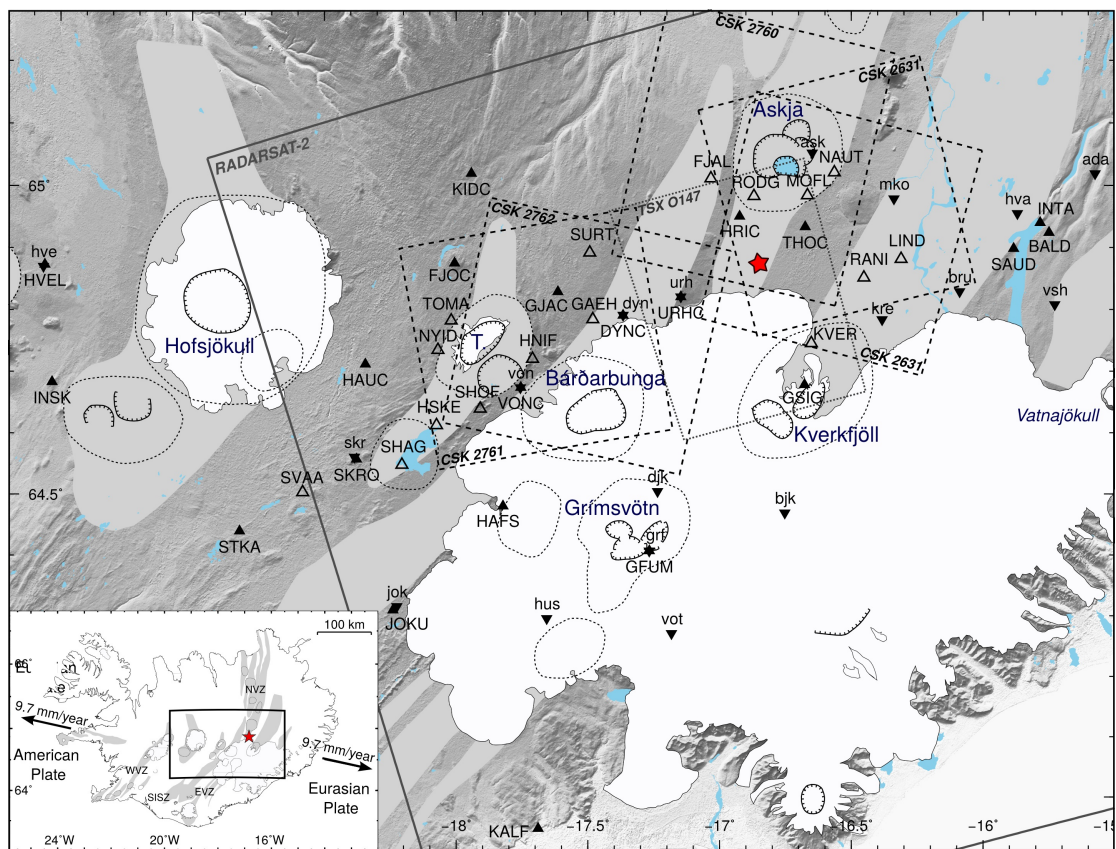
Extended Data item 1.

a

b
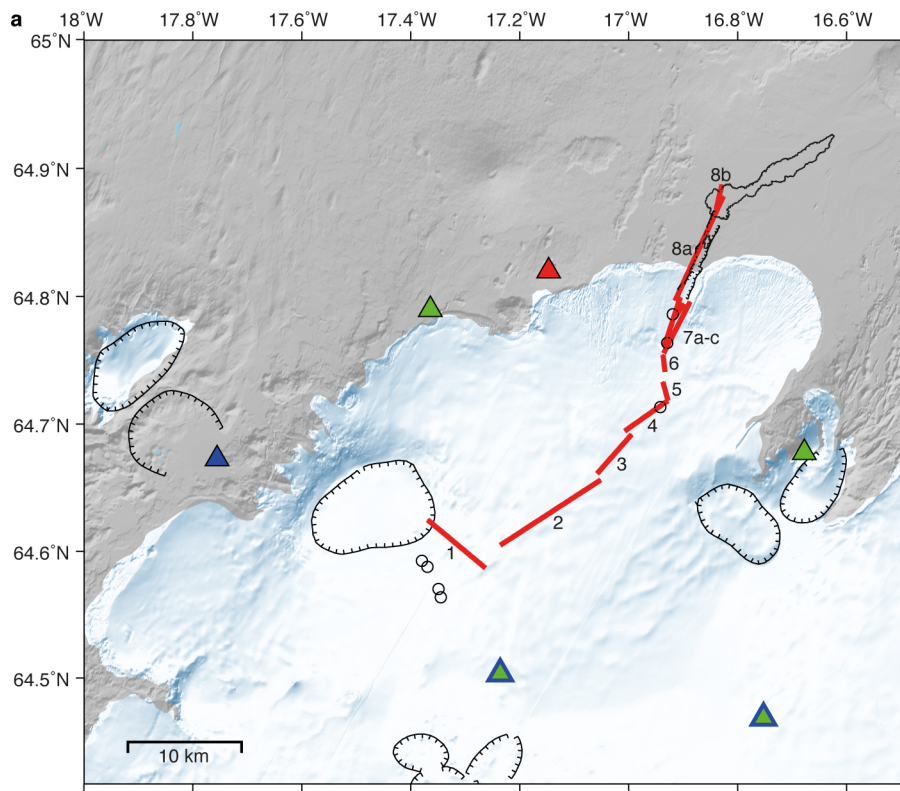
Nr	Lat1	Lon1	Lat2	Lon2	L	D	Strike	Dip	RMS	# Eq
	°N	°E	°N	°E	km	km	°	°	m	
1	64.6253	-17.3693	64.5873	-17.2630	5.2	0.0 – 7.5	127	89	177.7	71
2	64.6052	-17.2359	64.6566	-17.0515	10.0	3.5 – 6.5	55	87	103.8	343
3	64.6616	-17.0579	64.6923	-16.9947	4.6	4.0 – 7.0	219	89	118.6	365
4	64.6950	-17.0074	64.7189	-16.9279	4.8	3.0 – 7.5	53	89	81.2	427
5	64.7189	-16.9279	64.7336	-16.9371	1.7	5.0 – 6.5	-11	87	75.6	70
6	64.7414	-16.9334	64.7548	-16.9368	1.4	5.0 – 6.5	173	85	58.5	60
7a	64.7560	-16.9358	64.7963	-16.8873	4.9	5.0 – 7.0	47	87	82.6	404
7b	64.7611	-16.9349	64.7998	-16.9052	4.2	4.0 – 7.0	199	89	92.0	161
7c	64.7844	-16.9148	64.7949	-16.8987	1.1	6.0 – 7.0	35	83	69.9	215
8a	64.7970	-16.9150	64.8787	-16.8262	9.7	5.0 – 8.0	25	89	200.6	1181
8b	64.8685	-16.8393	64.8878	-16.8287	1.7	5.5 – 7.0	18	85	74.1	57

Extended Data item 2.

38

Bárðarbunga subsidence September 5, 2014
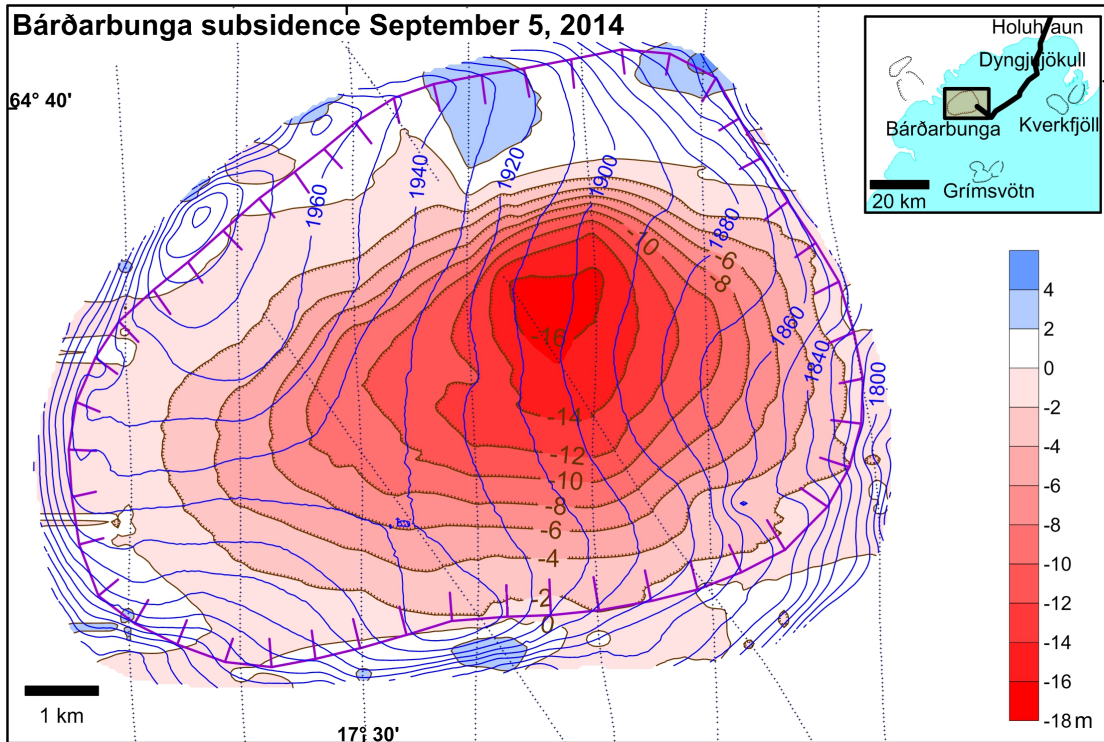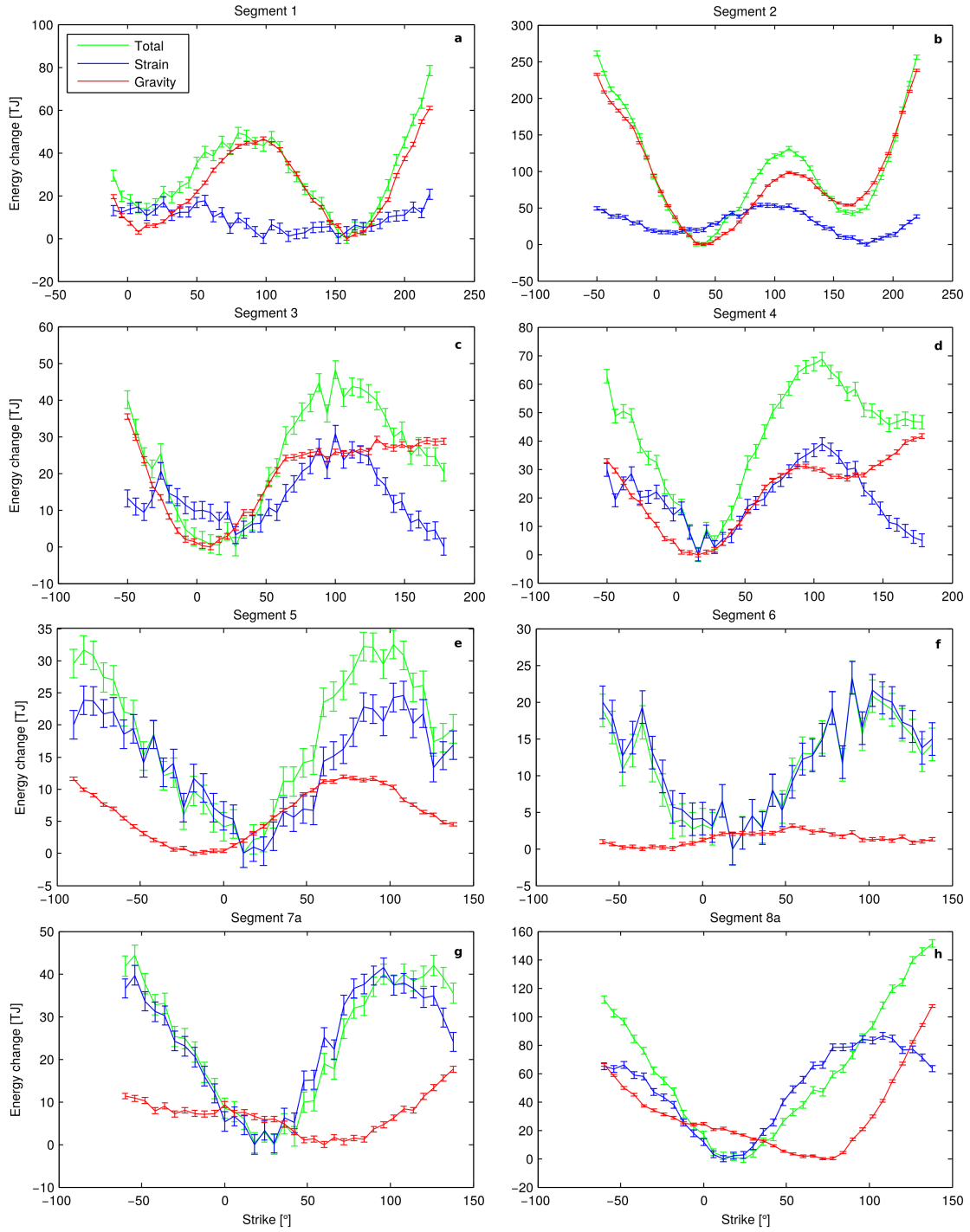
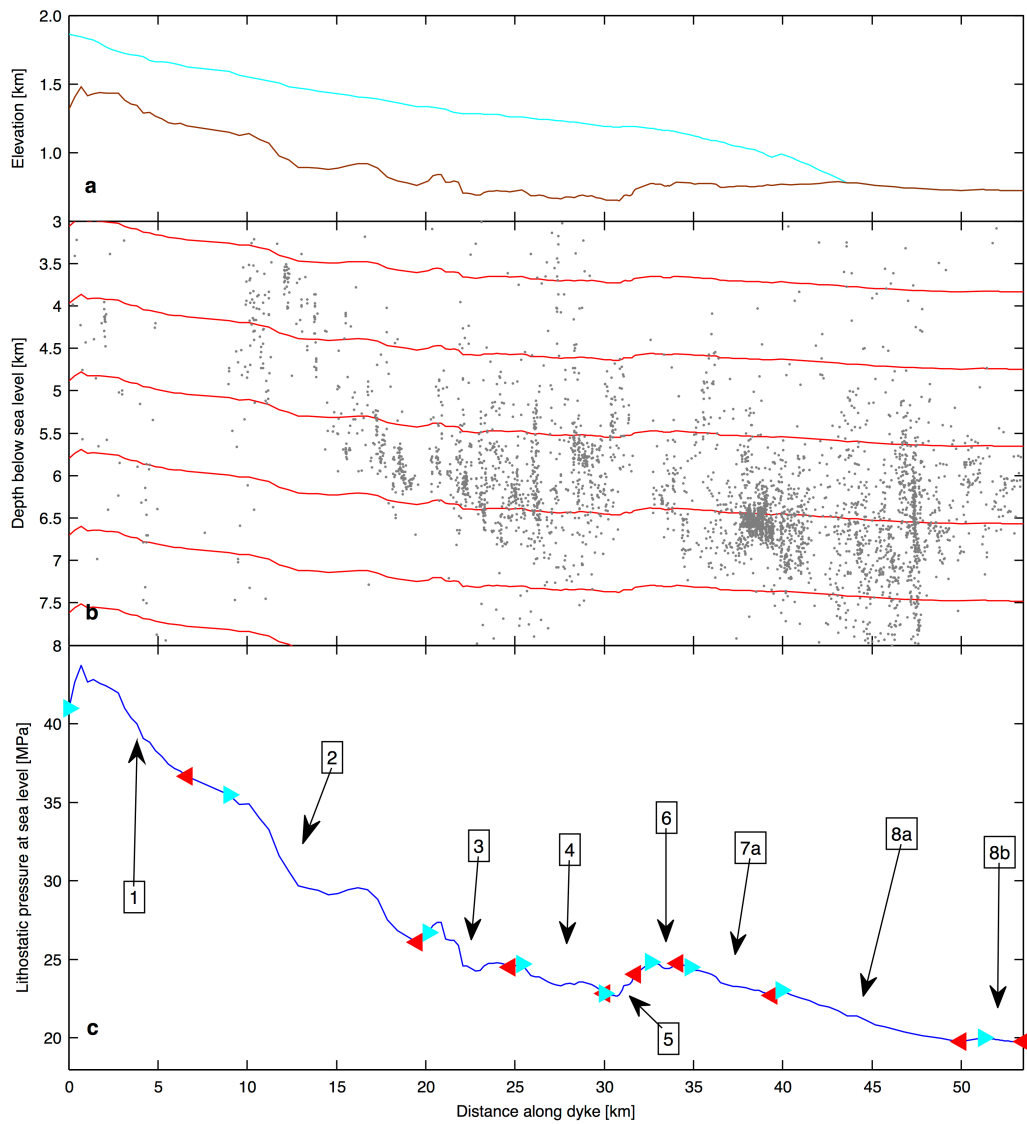**Extended Data item 3.**
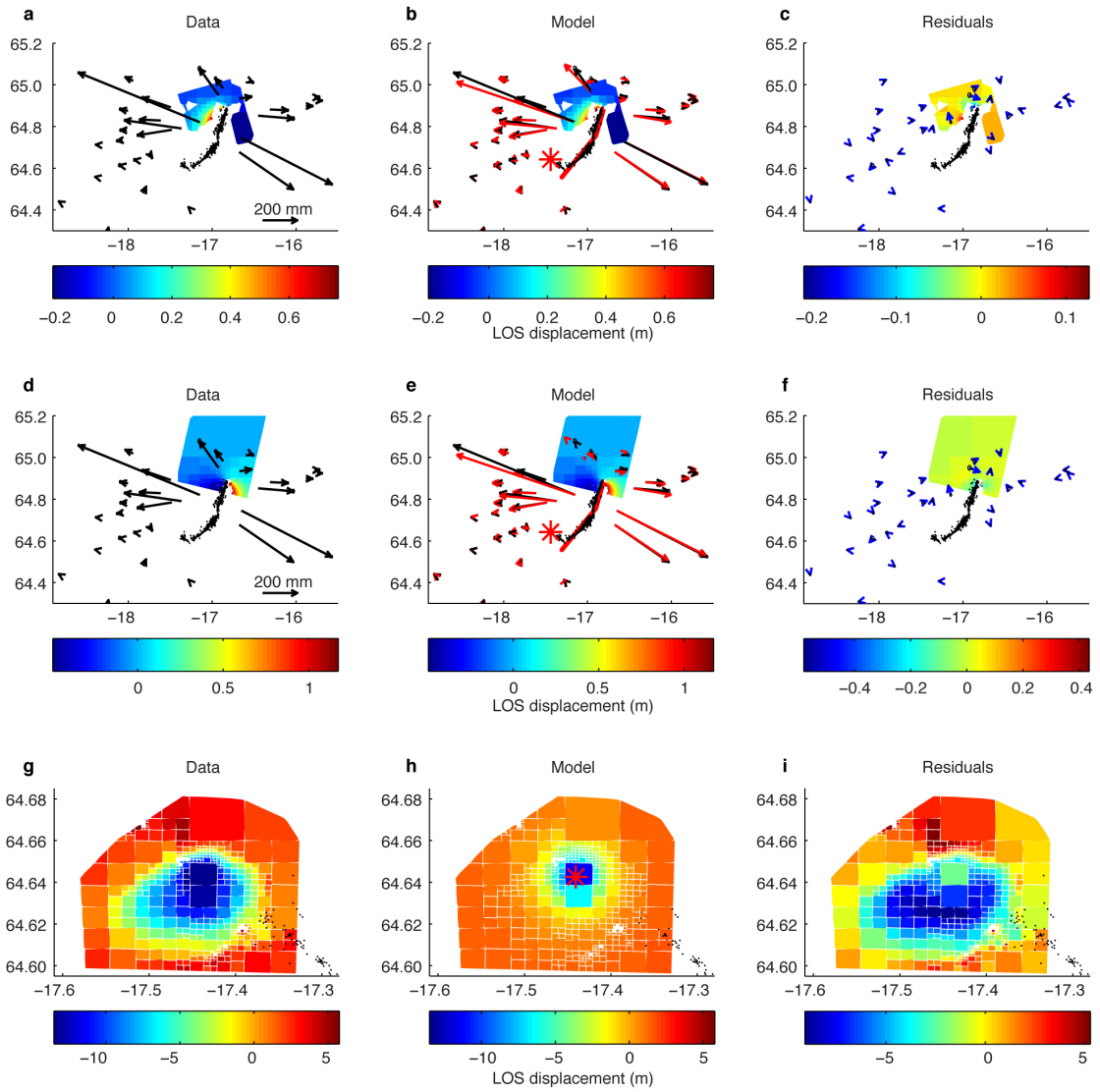
Extended Data item 4.
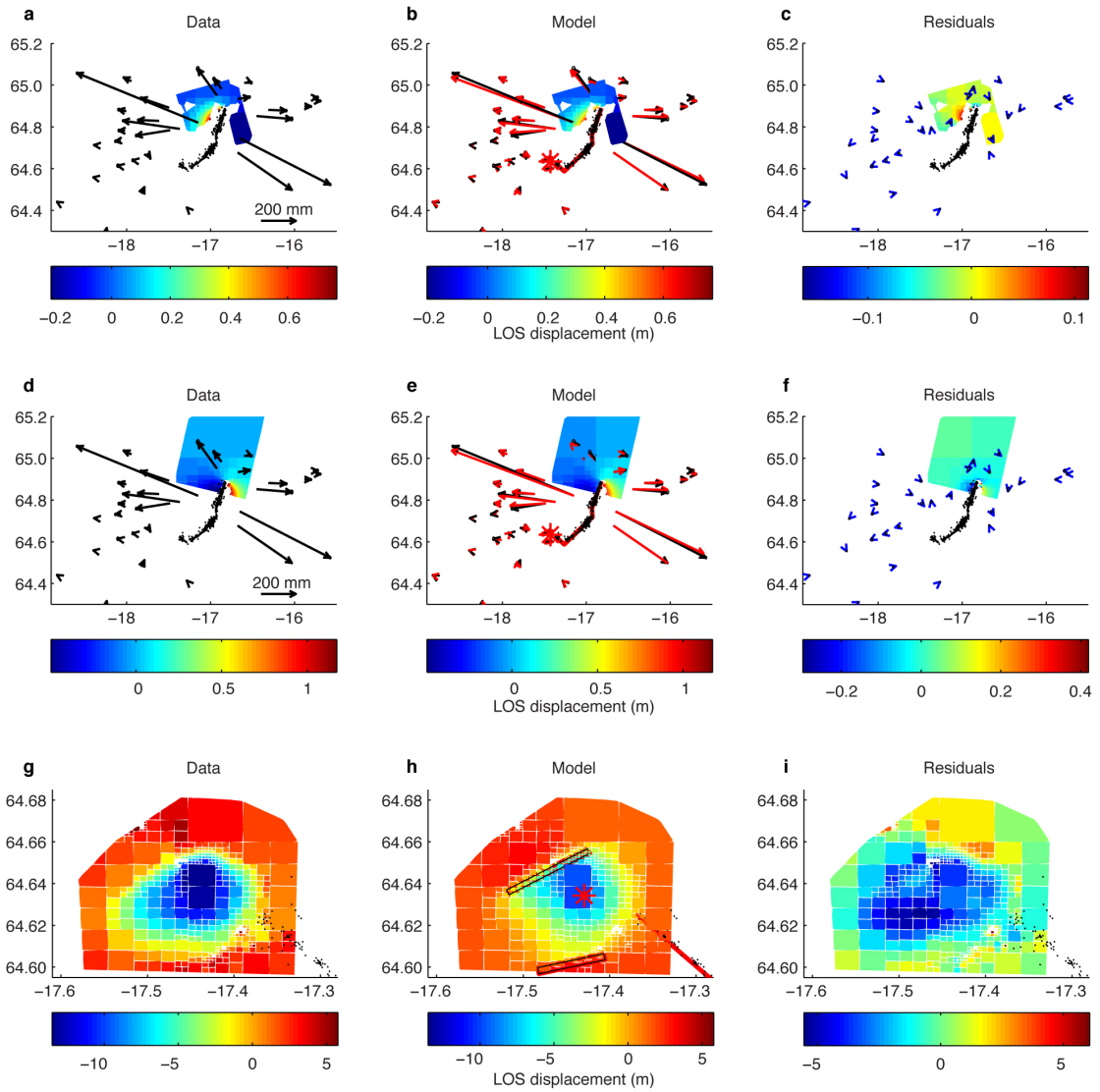
Extended Data item 5.

Extended Data item 6.

42
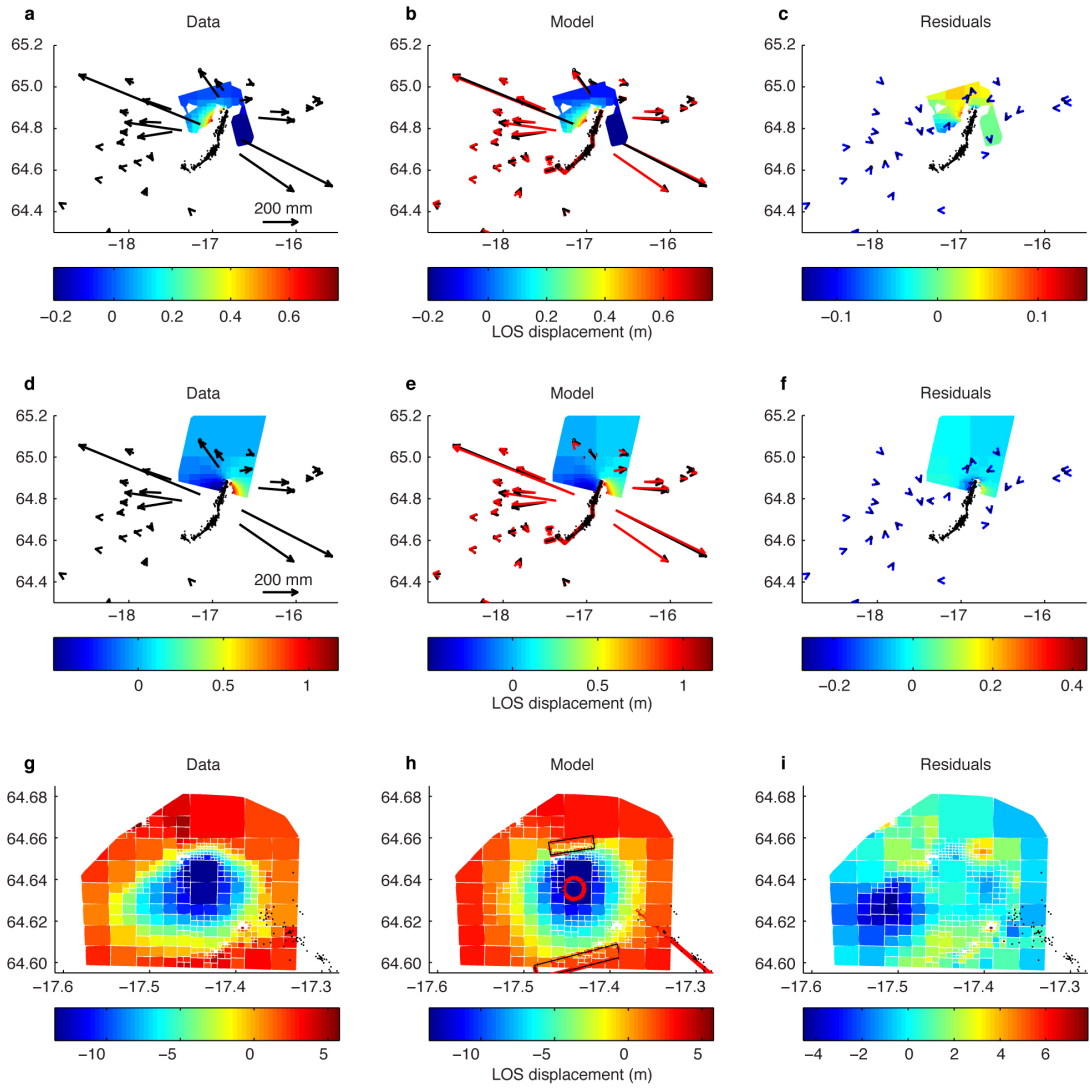
Extended Data item 7.

Extended Data item 8.

Segmented lateral dyke growth in a rifting event at Bárðarbunga volcanic system, Iceland

Supplementary Figure 1. Time series for selected continuous GPS sites

Supplementary Figure 2. Unwrapped interferograms

Supplementary Figure 3. Standard deviation of dyke opening

Supplementary Figure 4. Distribution of slip along the dyke

Supplementary Figure 5. Distribution of opening along the dyke for model 1

Supplementary Figure 6. Distribution of opening along the dyke for model 2

Supplementary Figure 7. Test of velocity model used for relocating earthquakes

Supplementary Figure 8. Error estimates for NonLinLoc earthquake locations.

Supplementary Table 1. Interferograms

Supplementary Table 2. Continuous GPS sites

Supplementary Table 3. Campaign GPS sites
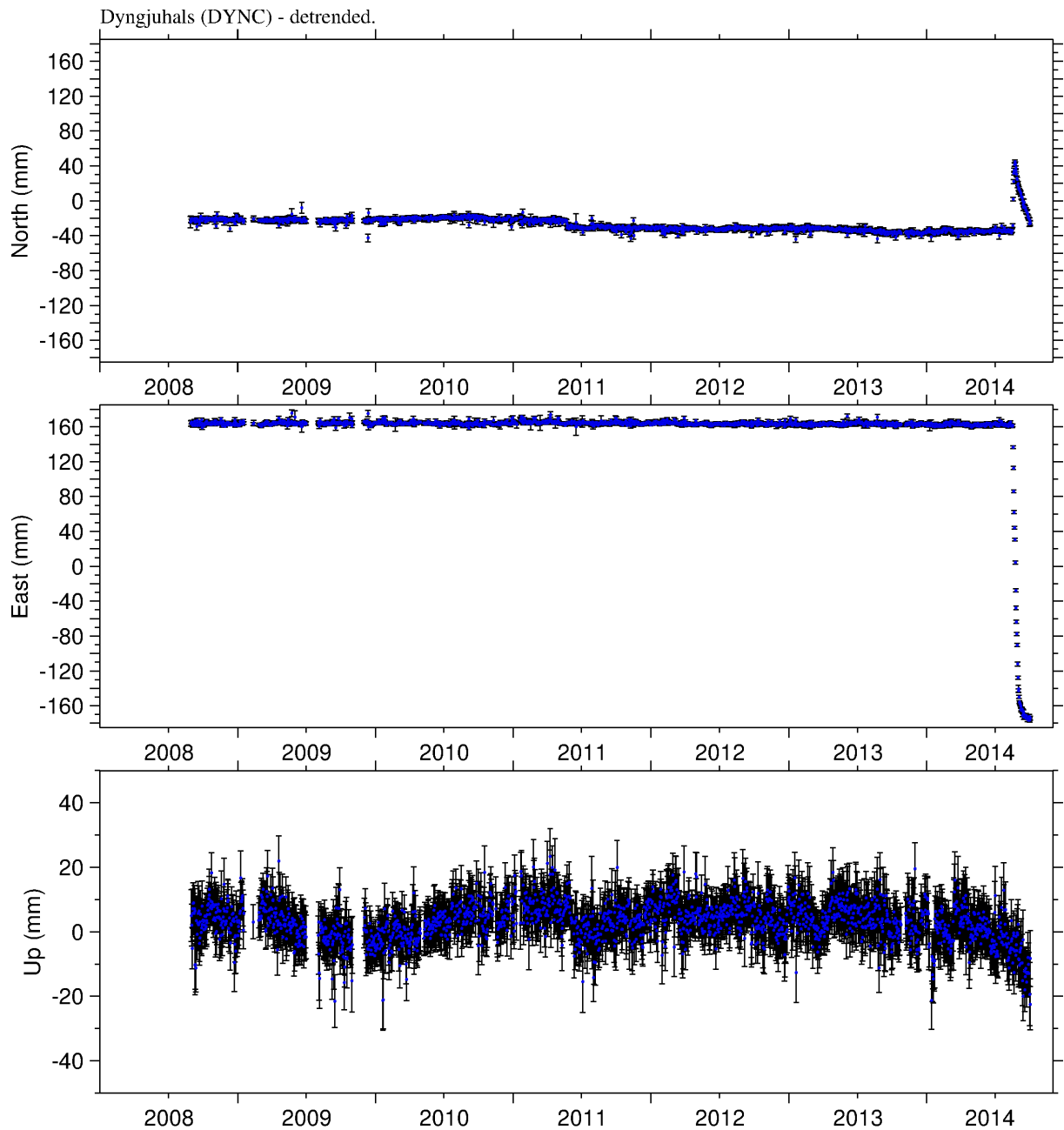
Supplementary Figure 1a: GPS time series for station Dyngjuháls (DYNC)
Each dot represents a 24 hour solution. The data were analysed in the ITRF08
reference frame and then detrended based on existing data prior to the Bárðarbunga
unrest. In 2011 the site moved south by 8± 2 mm during the Grímsvötn eruption, 43 km
south of the site.
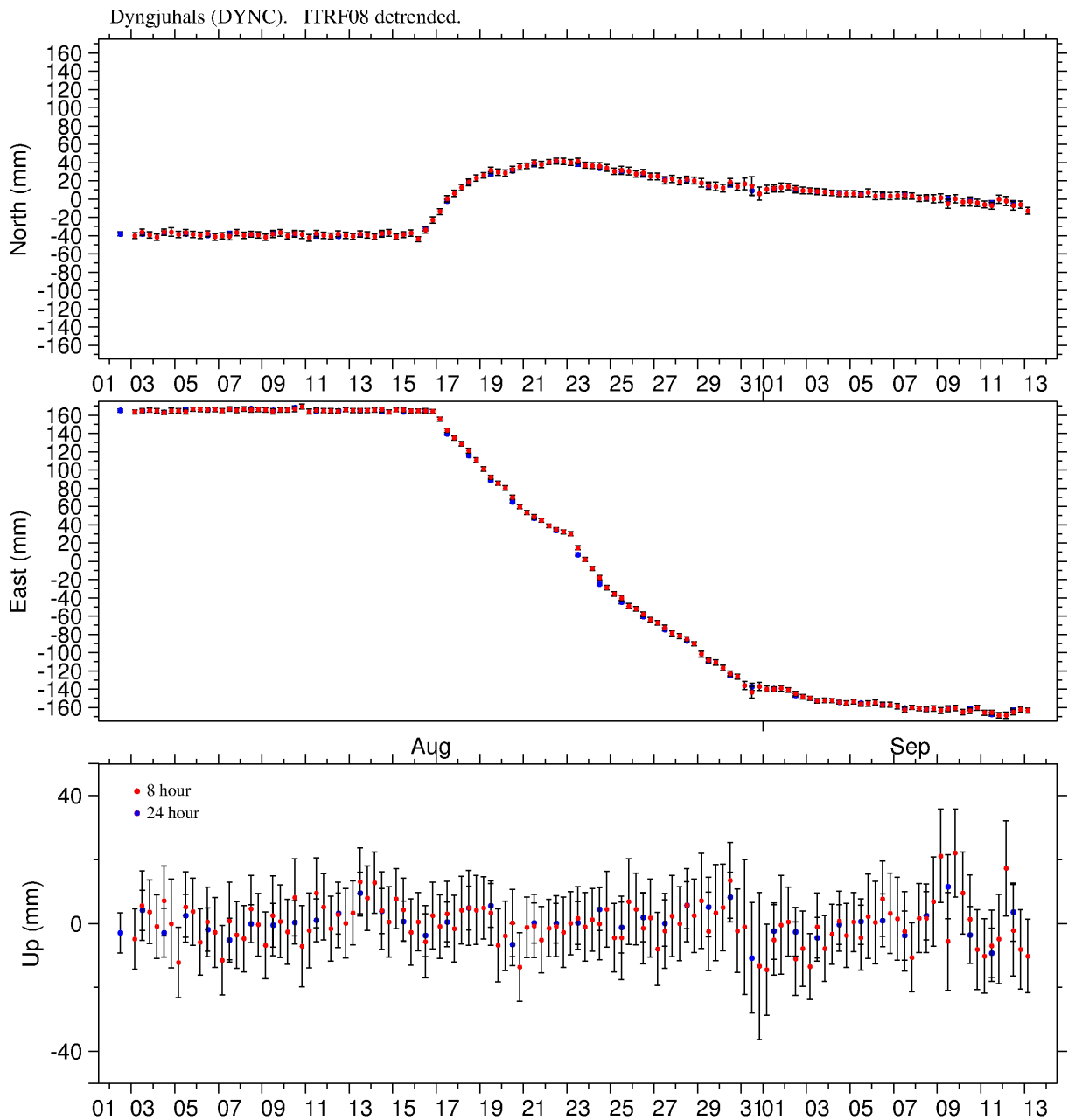
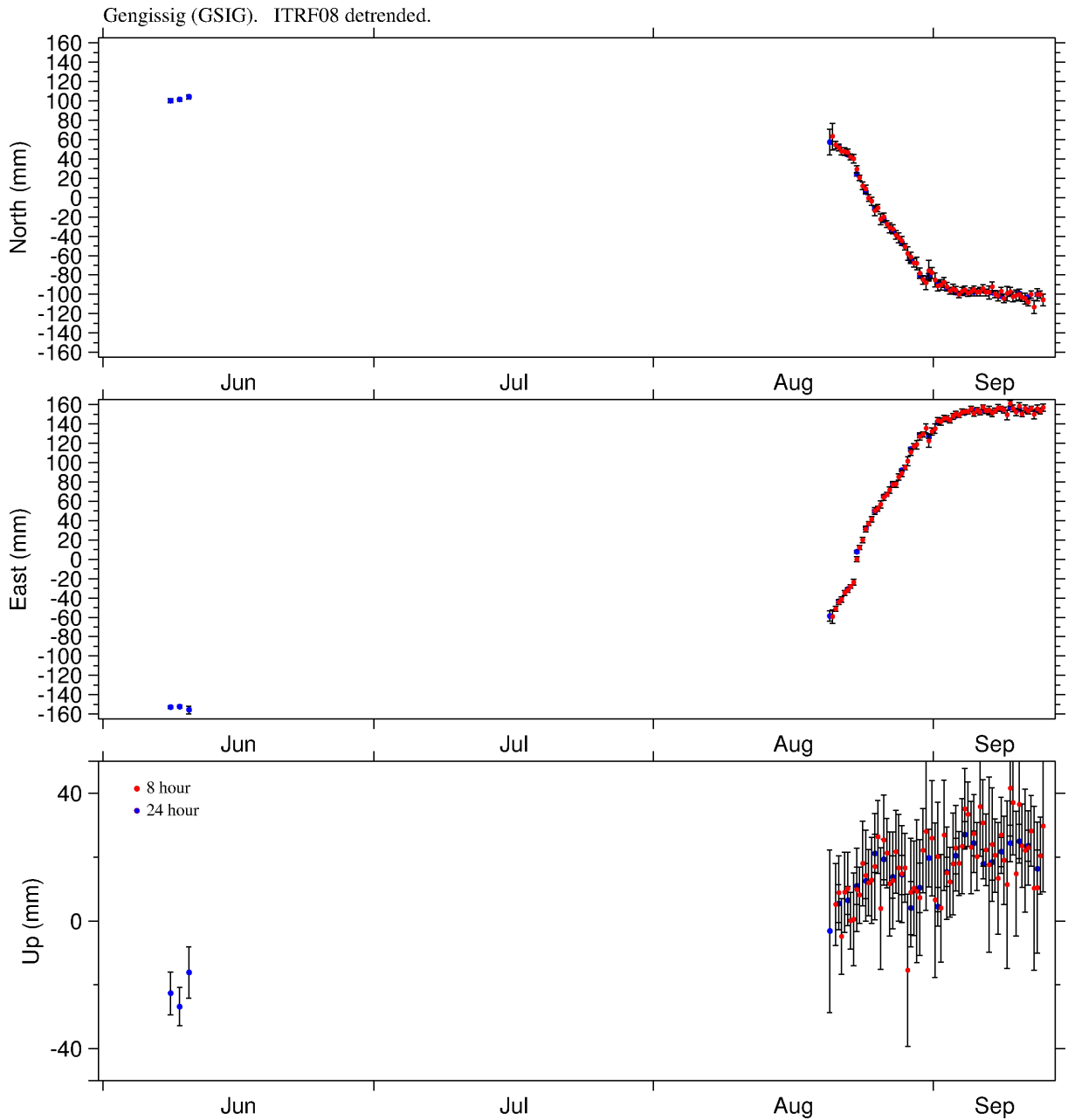**Supplementary Figure 1b: GPS time series for station Dyngjuháls (DYNC)**
Each blue dot represents a 24 hour solution and red dots show 8 hour solutions. The
site started moving on the 16 August. Little vertical deformation is apparent.

47
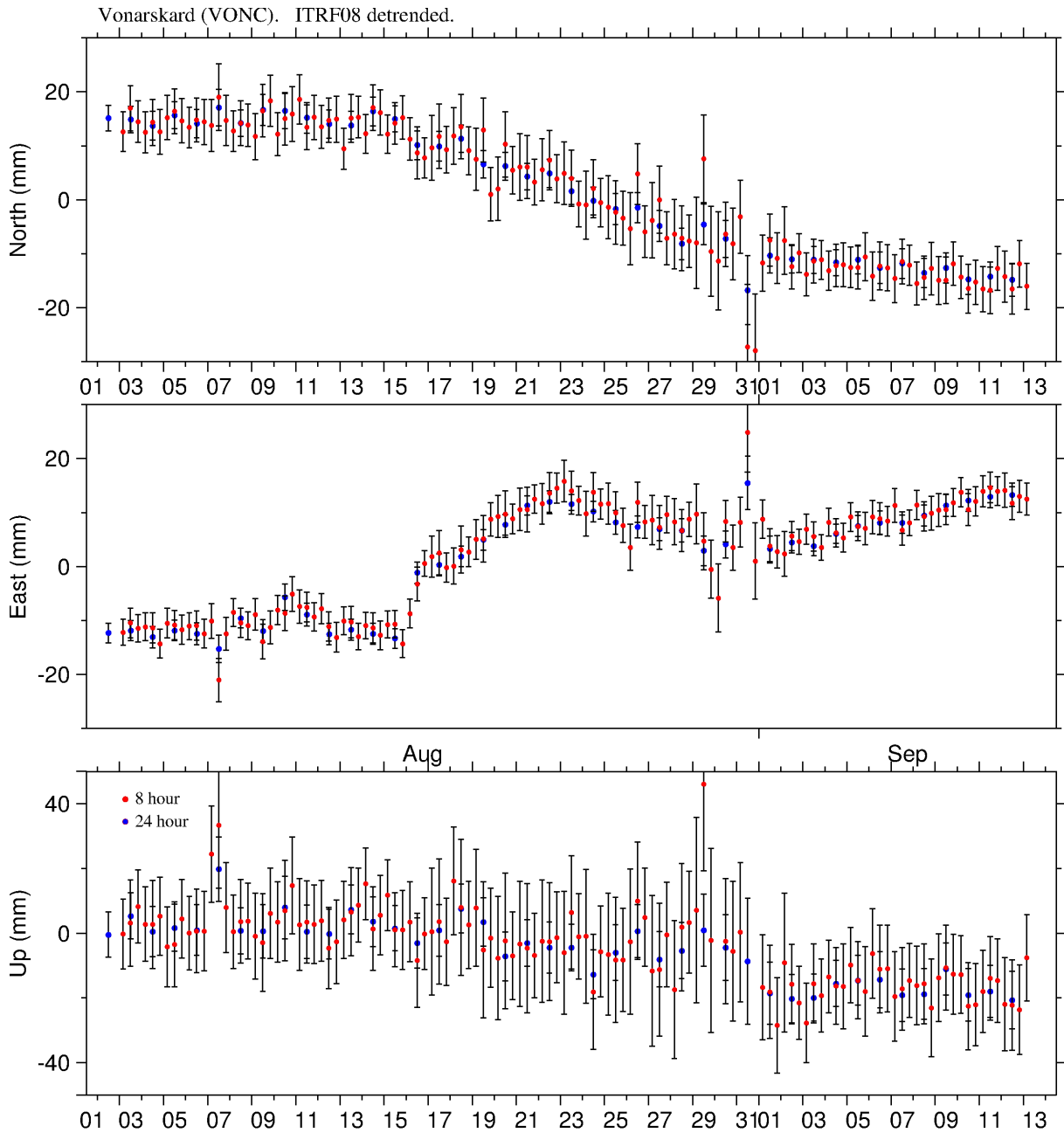
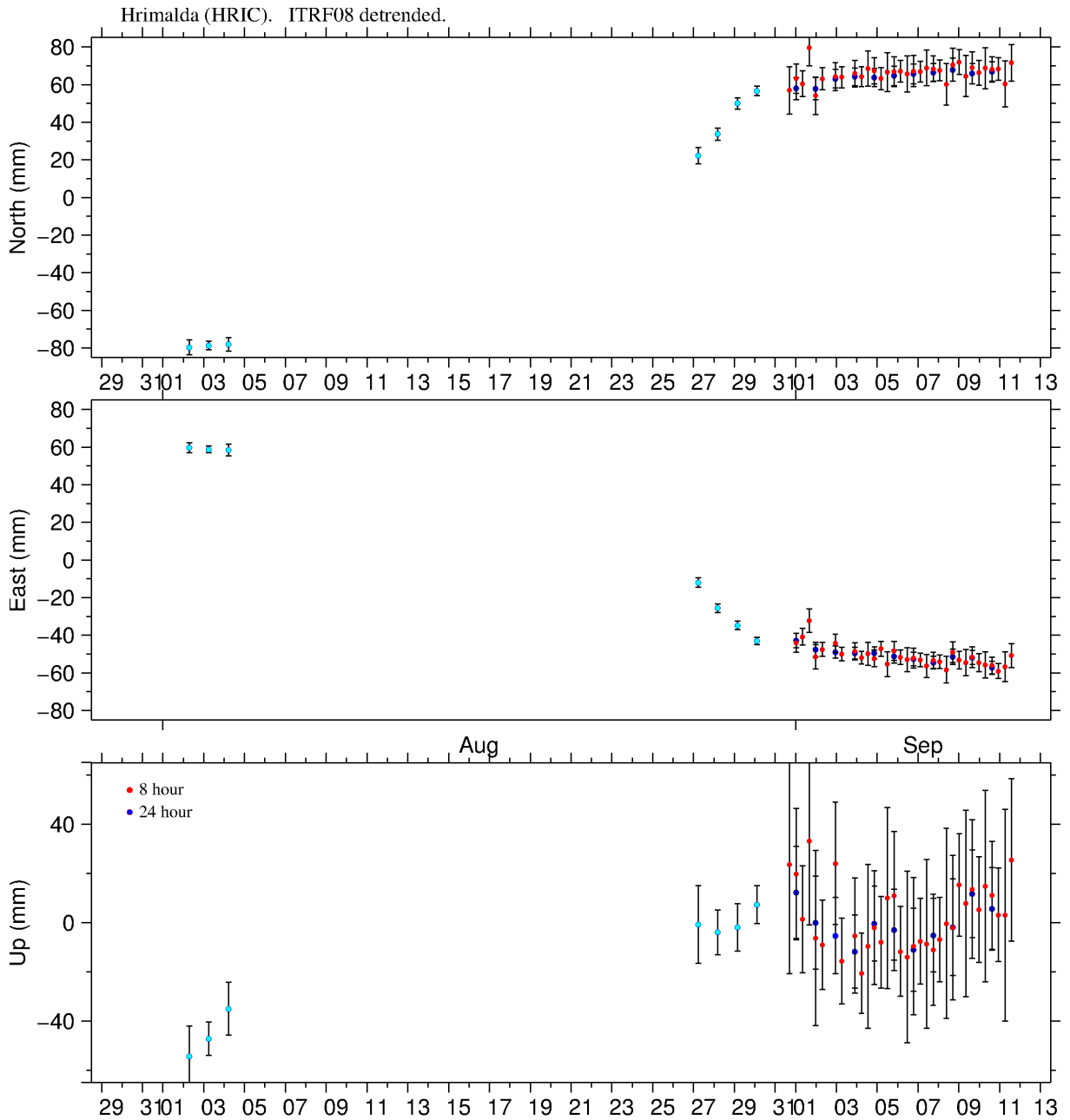**Supplementary Figure 1c: GPS time series for Vonarskarð (VONC)**
Each blue dot represents a 24 hour data solution and the red dots show 8 hour solutions.
The site started moving on the 16 August. The site can be sensitive to snow and icing
conditions as was observed on 31 August.

Gengissig (GSIG). ITRF08 detrended.

Supplementary Figure 1d: GPS time series for station Gengissig in Kverkfjöll (GSIG)

A permanent monument was installed and measured in June 2014 at this site, providing a reliable pre-unrest measurement at this location.

Supplementary Figure 1e: GPS time series for Hrímalda (HRIM & HRIC)
The station lies just northwest of the dyke tip. The aqua coloured points correspond to campaign measurements carried out in early and late August at the site HRIM, located within four meters of the new continuous station HRIC. This allows an estimate of the displacement range since the beginning of the unrest.

Urdarhals (URHC).   ITRF08 detrended.
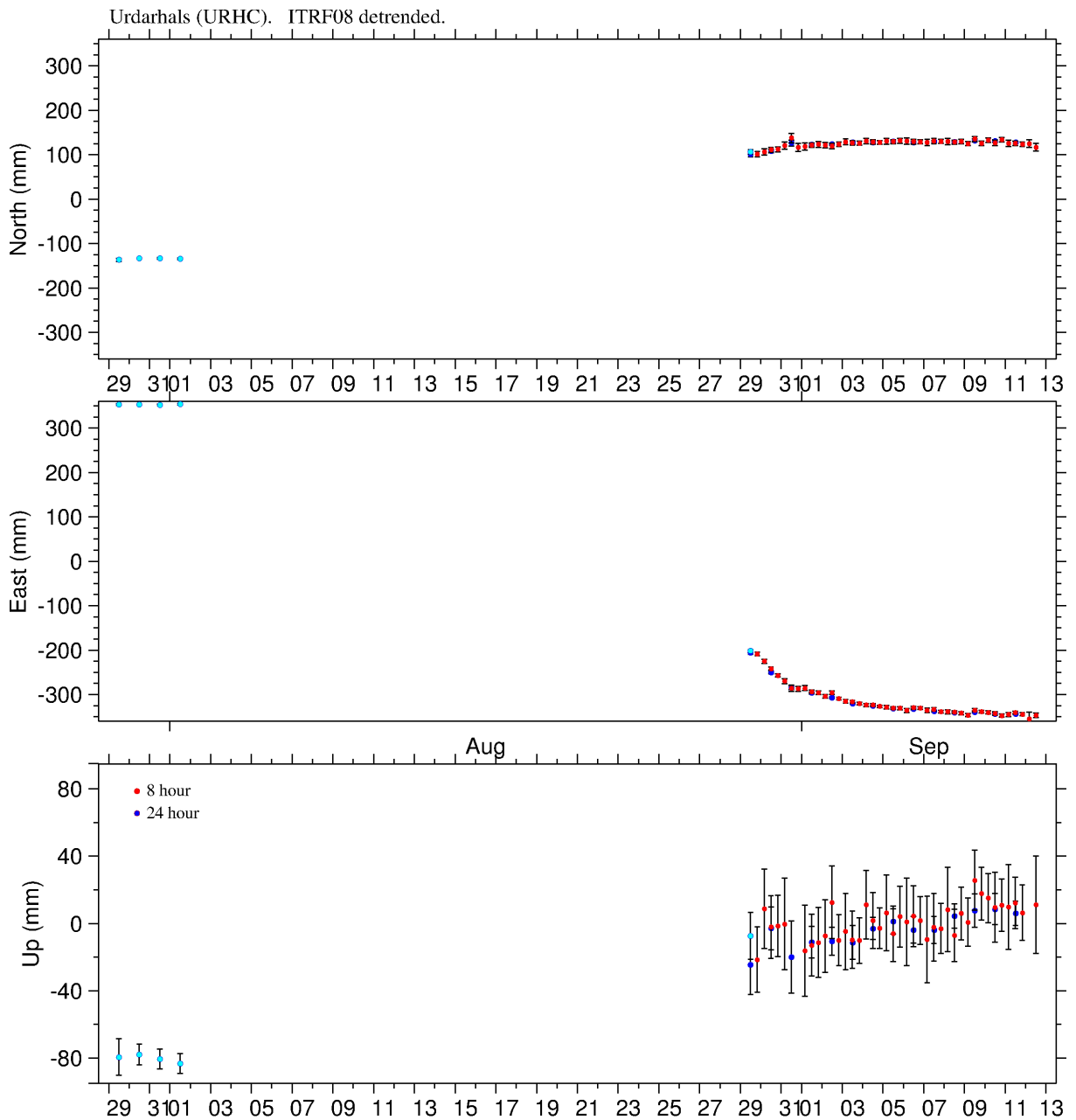
Supplementary Figure 1f: GPS time series for station Urðarháls (URHA & URHC)

The station URHC is north of Vatnajökull and was installed 2 m from the campaign site URHA. Data points are displayed with the same colour code as for station HRIC. This GPS site showed the most rapid deformation, due to its vicinity to the dyke intrusion (12 km). From the beginning of the unrest until 6 September, the extension between URHC and KVER was 1.30 m.

51
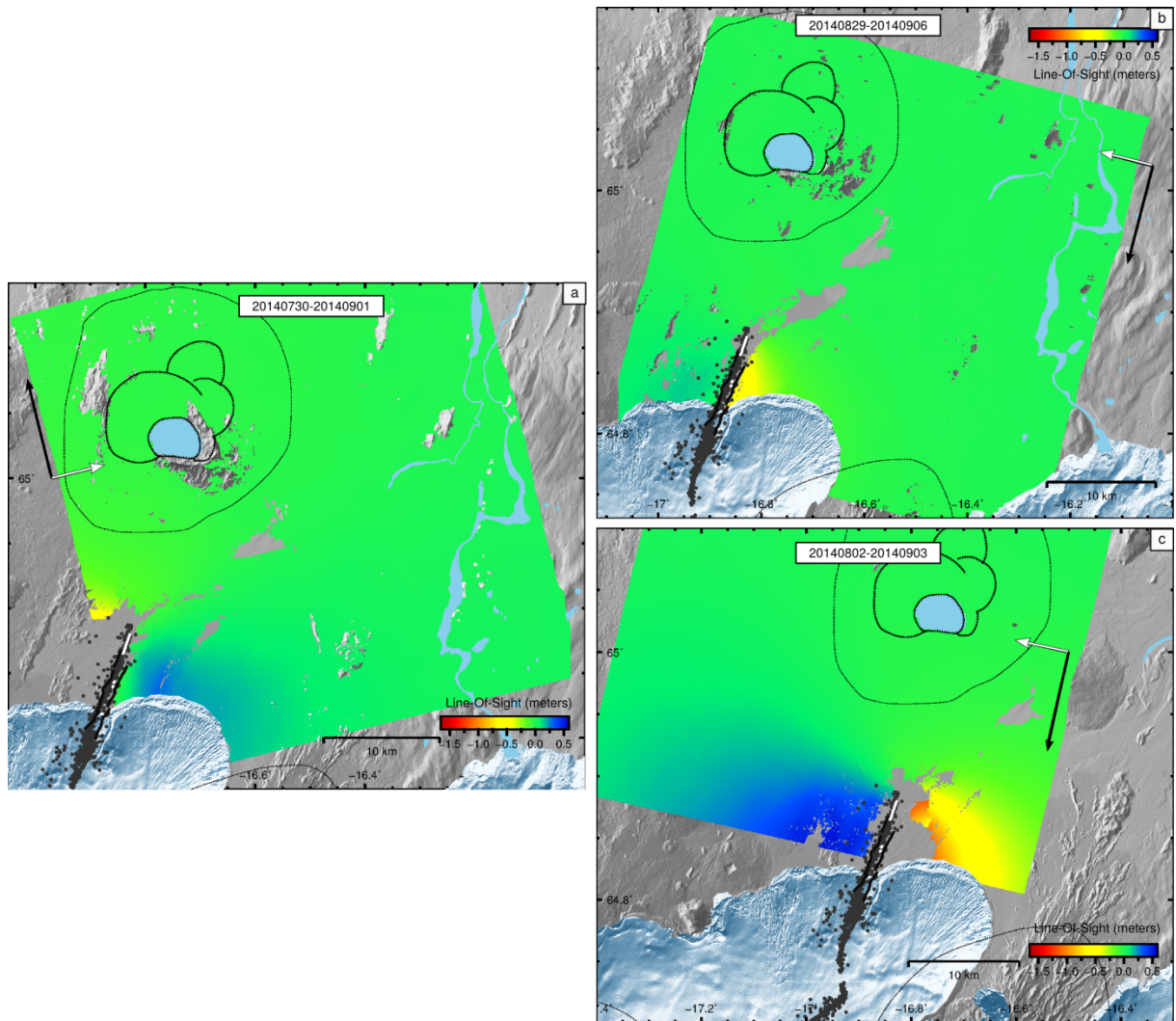
Supplementary Figure 2a: Unwrapped interferograms covering the dyke area
(above)

Interferograms used for modelling the surface deformation highlight the dyke intrusion leading to the eruption at Holuhraun for the time periods 2014/07/30-2014/09/01 (a), 2014/08/29-2014/09/06 (b) and 2014/08/02-2014/09/03 (c), respectively. These interferograms were produced from COSMO-SkyMed SAR images, the details of which are presented in Supplementary Table 3. Gray circles correspond to relocated earthquakes, the dark lines the boundaries of the dyke-induced graben and the white lines correspond to the eruptive fissure.
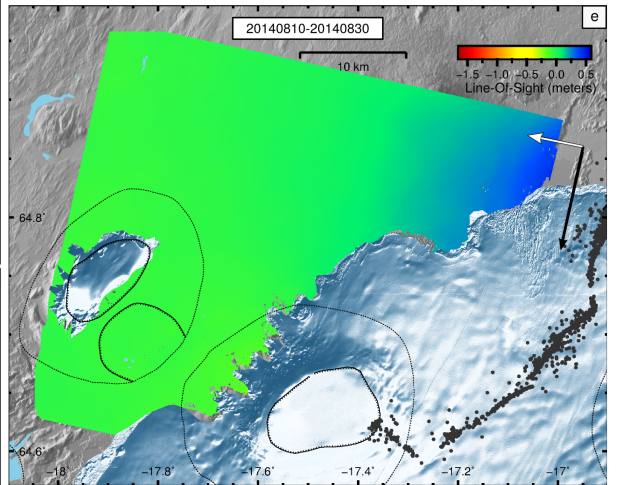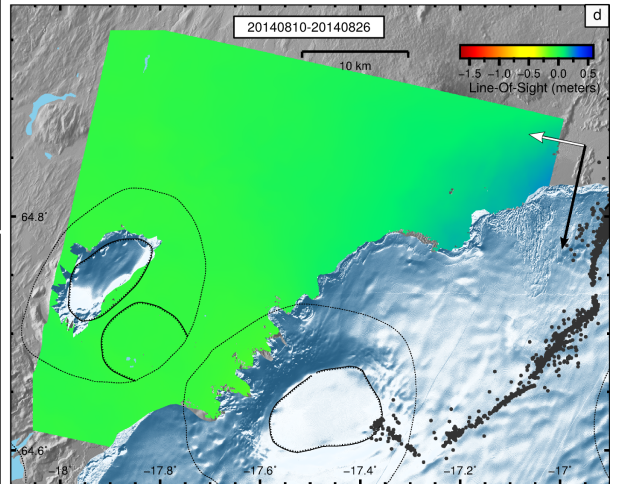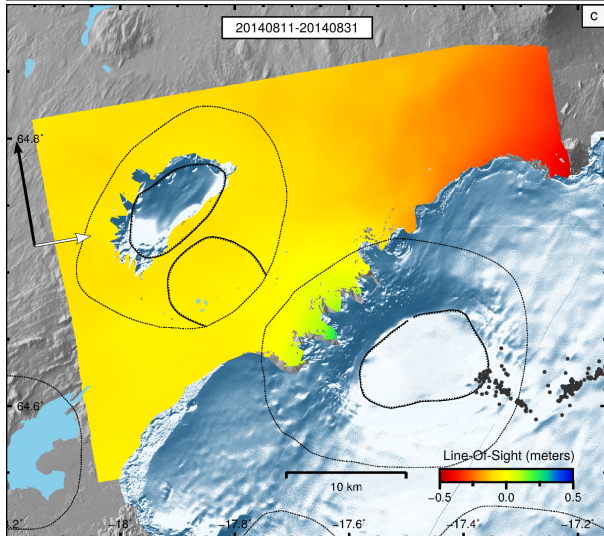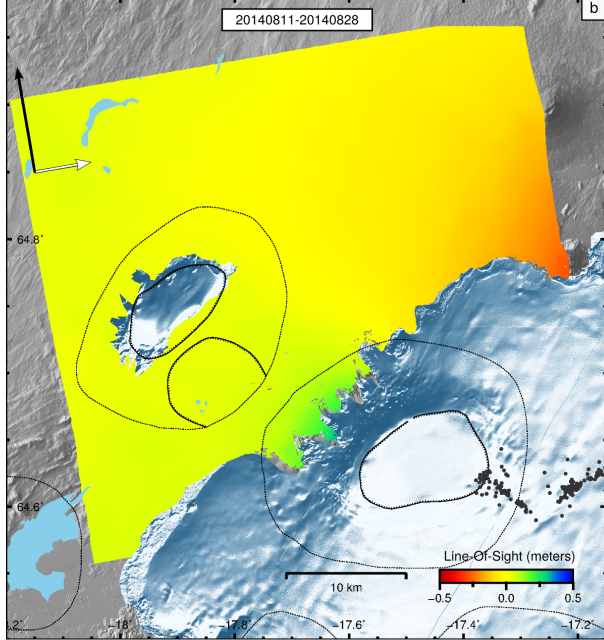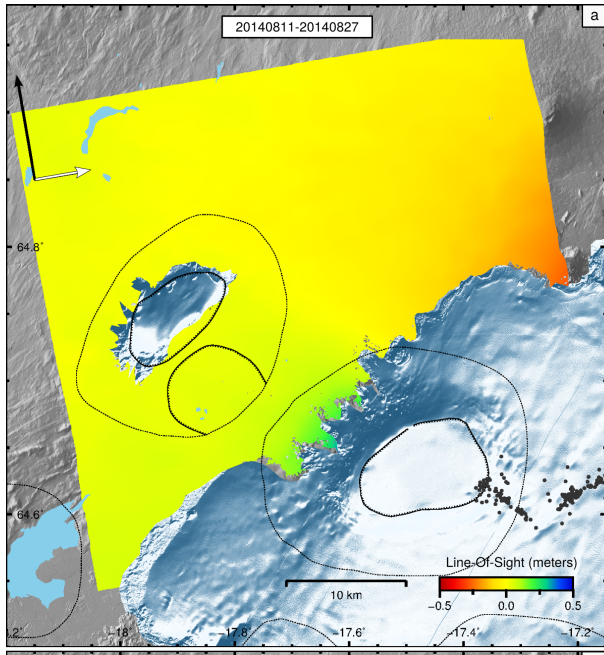
Supplementary Figure 2b: Unwrapped interferograms over Bárðarbunga area (see previous page)

Same as for the Supplementary Fig. 2a but with a focus on deformation occurring near the Bárðarbunga central volcano for the time periods 2014/08/11-2014/08/27 (a), 2014/08/11-2014/08/28 (b), and 2014/08/11-2014/08/31 (c) for the ascending configuration. The descending path is shown for the periods 2014/08/10-2014/08/26 (d), and 2014/08/10-2014/08/30 (e). Further details are provided in Supplementary Table 3.
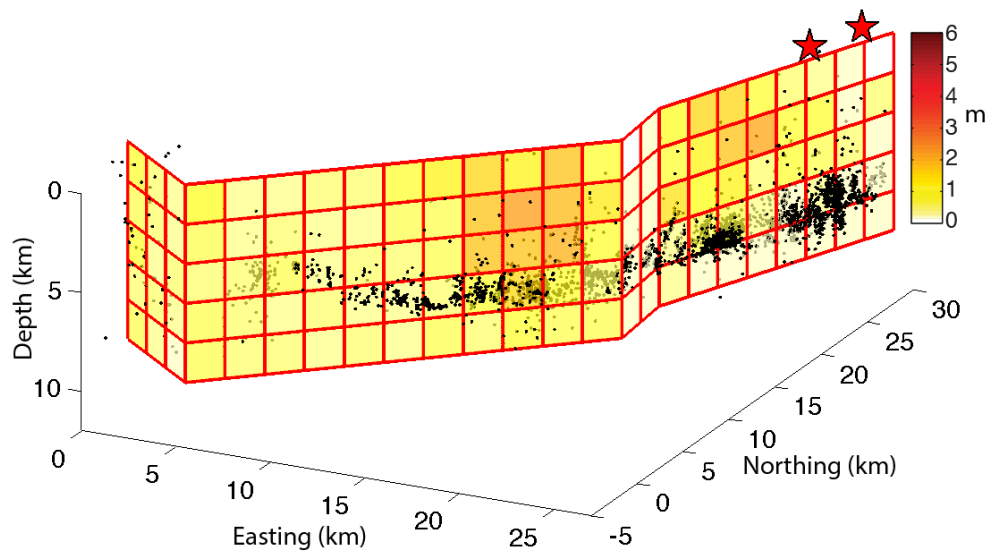
Supplementary Figure 3: Standard deviation of dyke opening
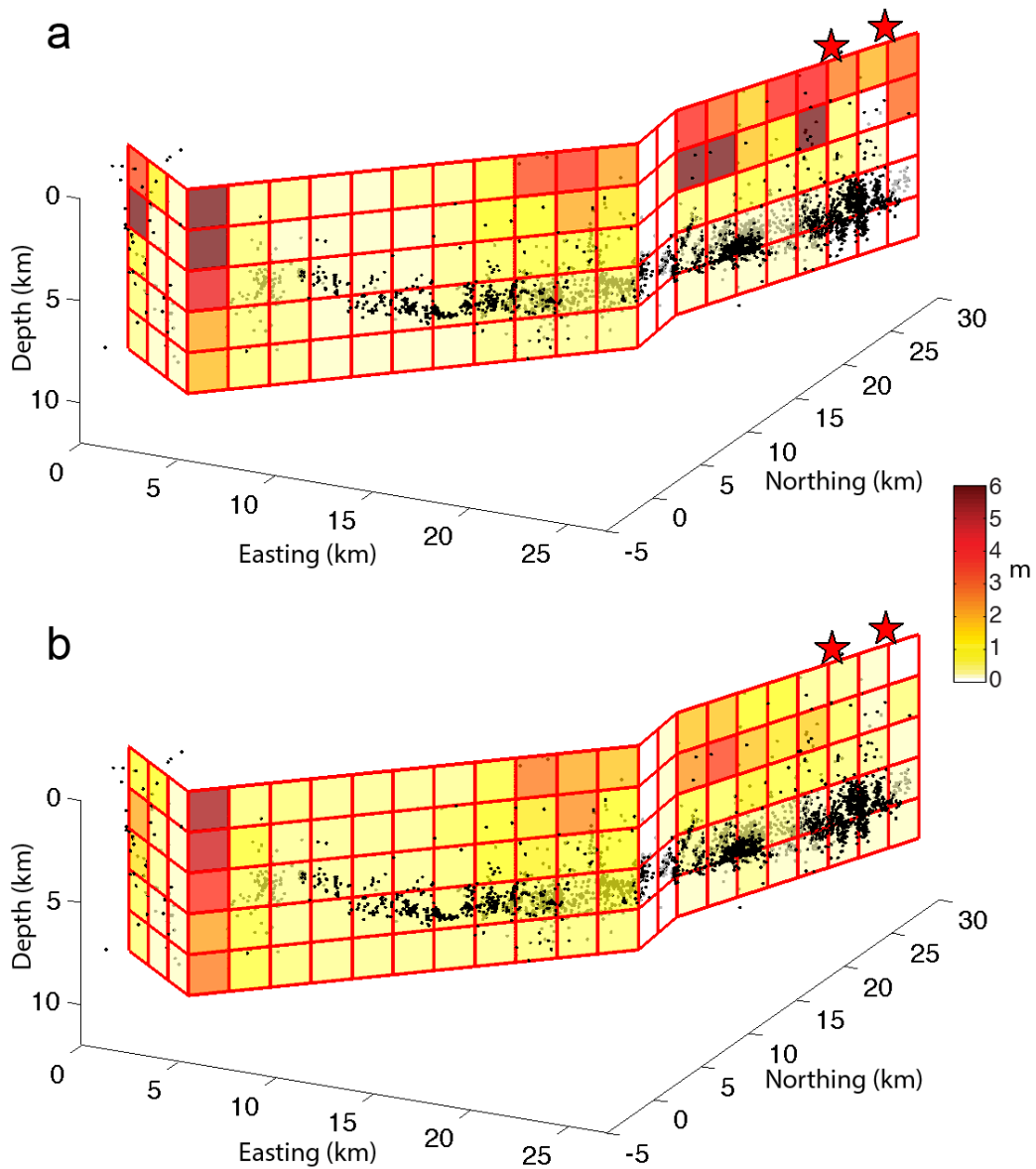Standard deviation of the posterior probability distribution for dyke opening, for the model shown in Fig. 3a of the main text, using a contracting point pressure source[39], two dip-slip faults beneath the caldera and a dyke modelled as four segments divided into multiple rectangular patches[37]. The data used are the same as those detailed in Extended Data Fig. 4, and the caldera subsidence data were not included.
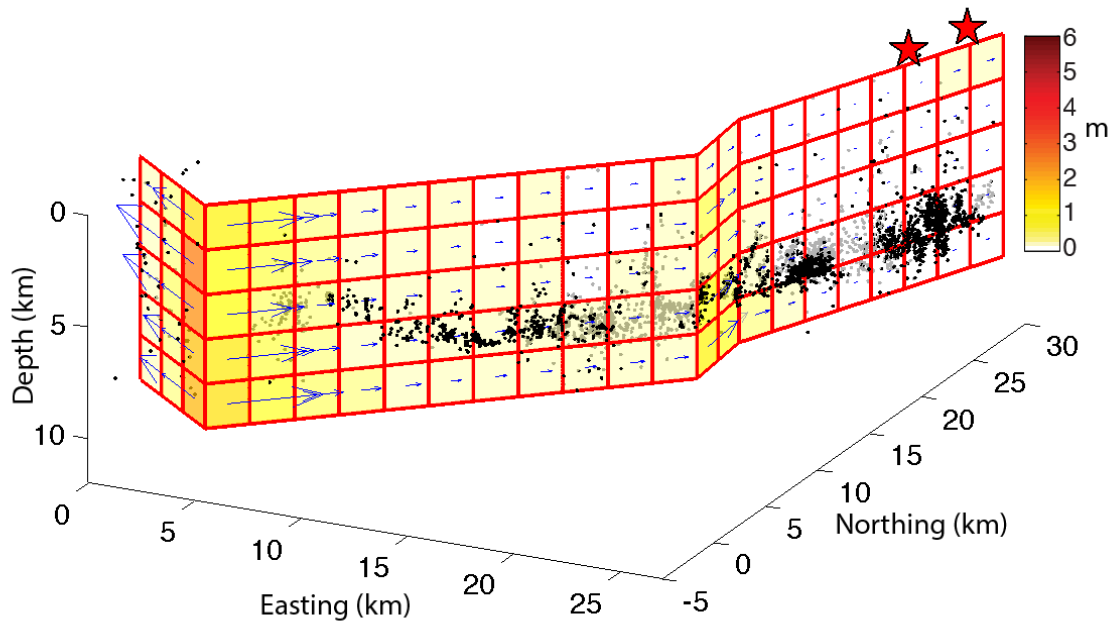
Supplementary Figure 4: Distribution of slip along the dyke
Median of the posterior probability distribution for slip, for the model shown in Fig. 3a of the main text, using a contracting point pressure source[39], two dip-slip faults beneath the caldera and a dyke modelled as four segments divided into multiple rectangular patches[37]. The data used are the same as those detailed in Extended Data Fig. 4, and the caldera subsidence data were not included. Colour indicates the magnitude of slip, and arrow lengths are scaled by the corresponding value.

Supplementary Figure 5: Distribution of opening along the dyke for model 1
Median values (a) and standard deviations (b) of the posterior probability distribution for dyke opening, for a model with a contracting point pressure source[39], two dip-slip faults beneath the caldera and a dyke modelled as four segments divided into multiple rectangular patches[37]. The large values of opening near the caldera are not significant, and likely an artefact of using a uniform pressure source to model subsidence that is largely accommodated by slip on faults above. The data used are outlined in Extended Data Fig. 4, and the caldera subsidence data were included.
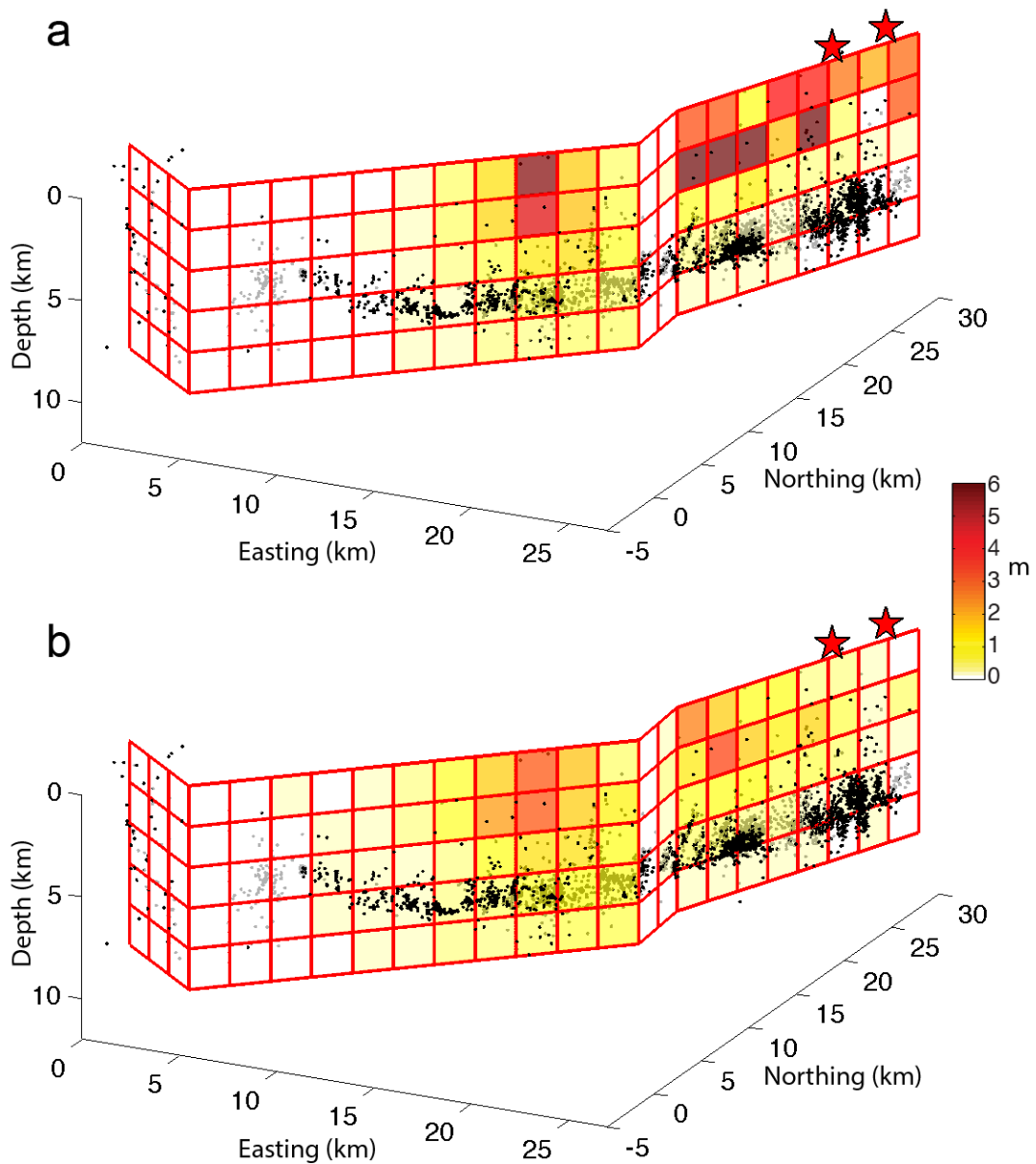
Supplementary Figure 6: Distribution of opening along the dyke for model 2
Median values (a) and standard deviations (b) of the posterior probability distribution,
for a model with a deflating penny-shaped crack[38] (used to represent the top of a flat-
topped chamber[48]), two dip-slip faults beneath the caldera and a dyke modelled as
four segments divided into multiple rectangular patches[37]. The data used are detailed
in Extended Data Fig. 4, and the caldera subsidence data were included.
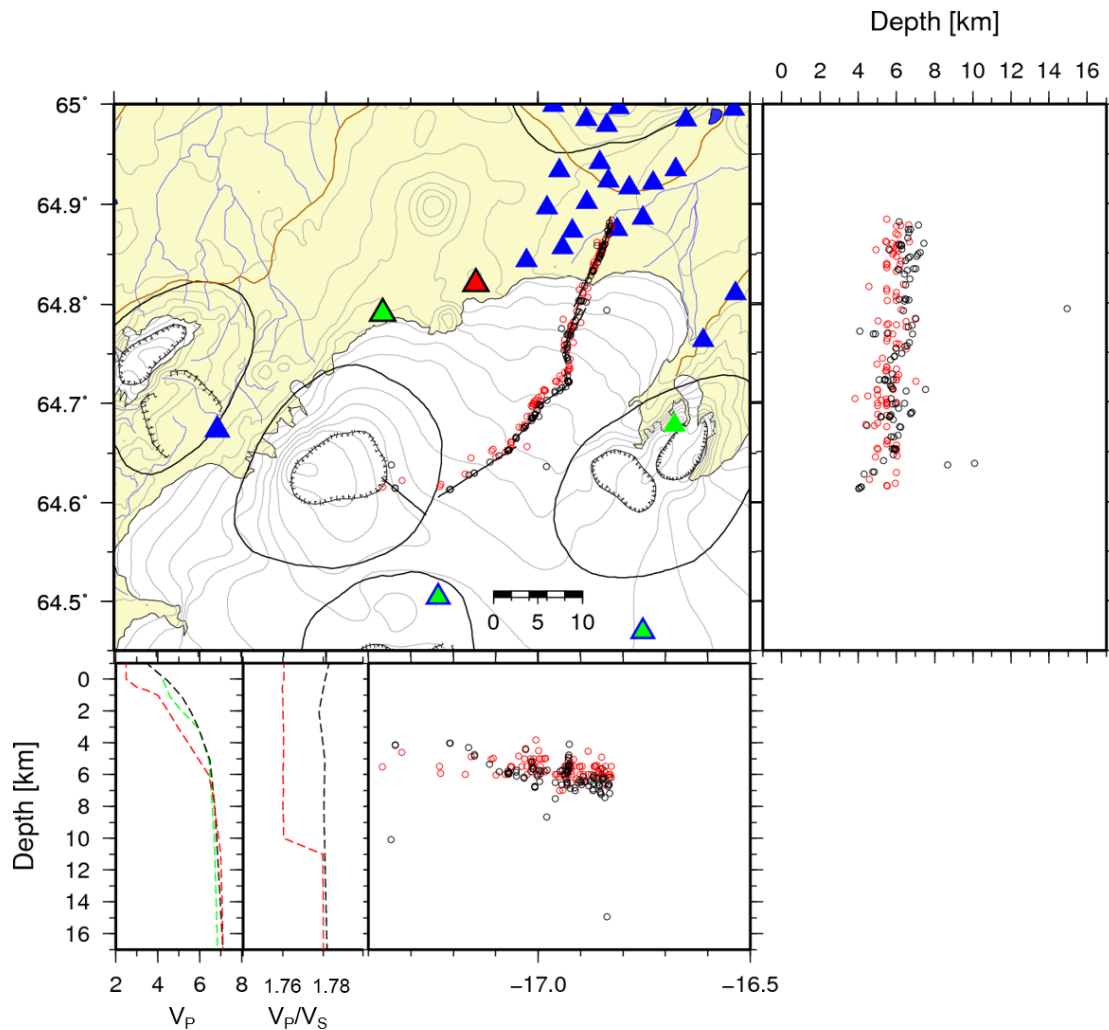
Supplementary Figure 7: Test of the velocity model used for relocating earthquakes

To test the absolute accuracy of the relatively located events, one hundred events with magnitudes around 2.5 and with good signal-to-noise ratios were selected for comparison with single event locations using the NonLinLoc code[25]. The figure shows the comparison of results from the two methods in map view and on two vertical cross sections. The relative locations (black circles) were estimated using the standard IMO SIL velocity model, while the single event locations (red circles) were estimated using the velocity model adapted from the Vatnajökull region of the ICEMELT profile. The horizontal distribution of the events compare rather well. Only small deviations occur at the location of dyke segment 4. The relative locations are generally deeper than the single event locations, but the difference is mostly within a few hundred metres. The velocity models, SIL (black) and cam-vatnaj (red) are shown on the vertical cross section, as well as their V_p/V_s ratios. Also shown is the V_p velocity for a third model, IMO-vj (green), which has been used at IMO for locating events in the Vatnajökull region. Relative locations in this model are discussed in the main text. Triangles show seismic station locations: green are IMO stations (those with blue edges have seismometers from Cambridge); blue are Cambridge University stations; red is a University College Dublin seismometer; stations shown with edged symbols are telemetered to IMO at Reykjavik for real-time locations.
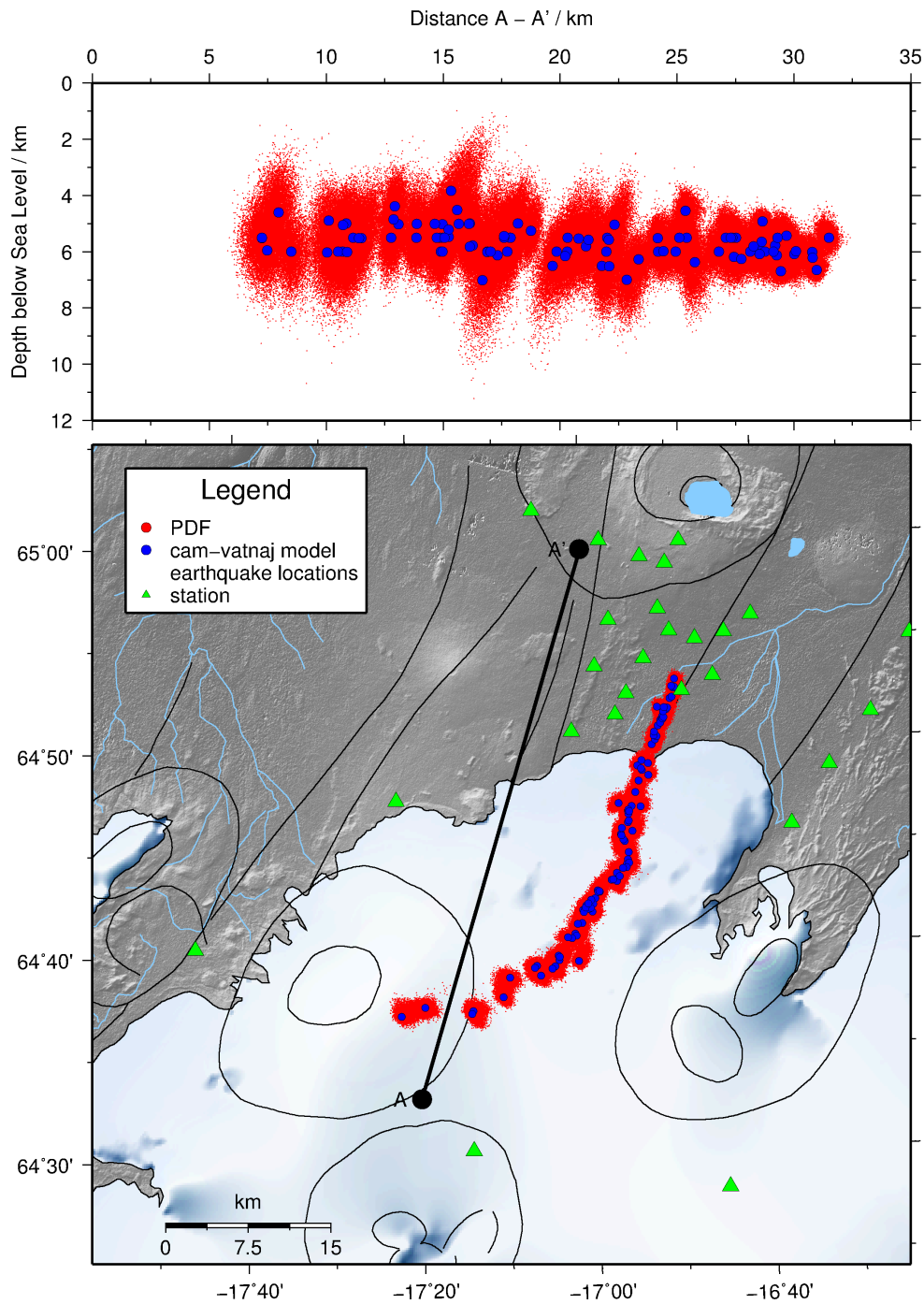
Supplementary Figure 8: Error estimates for the NonLinLoc earthquake locations.

Earthquake locations determined with NonLinLoc[25] (blue circles) shown with probability density functions (red dots); the higher the density of the dots, the greater the value of the PDF. The total distribution of the dots gives an approximation of the error ellipse for each event. Earthquakes are located using the cambridge-vatnajokull velocity model (cam-vatnaj). Stations used to locate the earthquakes are shown as green triangles.

SITE	Name	Cont. since	Lat (°)	Lon (°)	H (m)
KIDC	Kiðagil	01 Sep 2007	65.0192273	-17.9424339	935.1
HRIC*	Hrímalda	30 Aug 2014	64.9503900	-16.9240304	899.5
INTA	Inntakshús Kárahnjúkar	28 Nov 2007	64.9400093	-15.7828044	700.0
THOC*	Þorvaldshraun	30 Aug 2014	64.9337152	-16.6755862	750.0
BALD	Búrfellsalda	16 Nov 2008	64.9242637	-15.7492323	705.3
SAUD	Sauðárháls Norður	30 Oct 2004	64.8983982	-15.8837089	761.9
FJOC	Fjórðungsalda	03 Sep 2007	64.8749326	-18.0060490	1034.8
HVEL	Hveravellir	10 Aug 2006	64.8730401	-19.5612422	710.1
GJAC*	Gjallandi	27 Aug 2014	64.8287582	-17.6139334	918.4
URHC*	Urðarháls	29 Aug 2014	64.8203618	-17.1471516	1079.6
DYNC	Dyngjuháls	28 Aug 2008	64.7906182	-17.3662515	1208.5
HAUC	Háumýrar	02 Sep 2007	64.7114847	-18.3448169	726.4
INSK	Innri Skúti	14 Aug 2008	64.6828287	-19.5338452	776.4
GSIG*	Gengissig Kverkfjöll	20 Aug 2014	64.6780791	-16.6775253	1846.1
VONC	Vonarskarð	27 Aug 2013	64.6736094	-17.7544167	1082.3
SKRO	Skrokkalda	21 Sep 2000	64.5568268	-18.3782027	982.2
HAFS	Hamarinn	02 Jun 2013	64.4802608	-17.8220054	1619.4
STKA	Stóra Kjalalda	20 Aug 2006	64.4391888	-18.8221849	700.6
GFUM	Grímsfjall	2004	64.4067593	-17.2665955	1790.5
JOKU	Jökulheimar	30 May 2009	64.3095560	-18.2400092	740.4
KALF	Kálfafell	05 Aug 2012	63.9473298	-17.6888712	142.9

Supplementary Table 1: Continuous GPS sites
Continuous GPS stations used for modelling.
(*) Continuous stations installed and operated in response to the Bárðarbunga unrest. A permanent monument had been installed in June 2014 at GSIG but the other monuments were set up during the unrest within a few meters of existing benchmarks with long observation history.

SITE	Name	Obs Pre/Unrest	Lat (°)	Lon (°)	H (m)
NAUT	Nautahnútur	03Aug / 31Aug	65.0209220	-16.5640942	757.3
FJAL	Fjallsendi S	02Aug** / 02Sep	65.0112421	-17.0329182	920.4
MOFL	Móflöt	09Aug/ 31Aug	64.9839824	-16.6667443	787.8
RODG	Roðgúll	09Aug / 30Aug	64.9828857	-16.8696116	1088.8
HRIM*	Hrímalda NA	03Aug / 27Aug	64.9504143	-16.9239802	898.5
THOR*	Þorvaldshraun	03Aug / 27Aug	64.9333500	-16.6750651	748.6
SURT	Surtluflæður	01Aug / 25Aug	64.8918380	-17.4926757	875.1
LIND	Lindasel	04Aug / 02Sep	64.8816508	-16.3110683	707.1
RANI	Kverkfjallarani	04Aug / 03Sep	64.8516244	-16.4521455	784.5
GJAL*	Gjallandi	01Aug / 24Aug	64.8286072	-17.6139862	916.9
URHA*	Urðarháls	01Aug / 25Aug	64.8203732	-17.1471230	1078.4
GAEH	Gæsahnjúkur	01Aug / 01Sep	64.7842224	-17.4813268	1063.2
TOMA	Tómasarhagi	01Aug / 24Aug	64.7821611	-18.0189058	871.8
KVER	Kverkfjöll	04Aug / 02Sep	64.7453578	-16.6519185	877.2
NYID	Nýidalur	01Aug / 24Aug	64.7344615	-18.0691153	867.6
HNIF	Hníflar	01Aug / 24Aug	64.7202135	-17.7102437	997.1
SHOF	Svarthöfði	31Jul / 24Aug	64.6390654	-17.9085973	991.4
HSKE	Hágöngusker	31Jul / 25Aug	64.6121352	-18.0747508	908.4
SHAG	Syðri Háganga	31Jul / 24Aug	64.5476363	-18.2061570	898.1
SVAA	Svartá	31Jul / 24Aug	64.5029058	-18.5826969	684.4

Supplementary Table 2: Campaign GPS sites
Campaign GPS sites used for modelling. The third column shows the last pre-unrest data point and the first occupation during unrest.
(*) New monuments were installed next to four sites and operated continuously in response to the Bárðarbunga unrest.
(**) Due to receiver failure this site only logged L1 data during the pre-unrest campaign. However, the site had a good occupation history prior to 2014 and was last measured in 2013.

Satellite	Dates	Orbit	B_p (m)	Path	Mean incidence angle	Look direction
CSK	20140730-20140901	2631	439	ASC	29.47	76.05
CSK	20140813-20140829	2631	-426	DESC	27.38	-75.45
CSK	20140829-20140906	2631	288	DESC	27.38	-75.45
CSK	20140802-20140903	2760	-63	DESC	34.07	-77.12
CSK	20140811-20140831	2761	-156	ASC	44.56	80.31
CSK	20140811-20140827	2761	-241	ASC	44.56	80.31
CSK	20140811-20140828	2761	-195	ASC	44.56	80.31
CSK	20140827-20140828	2761	-46	ASC	44.56	80.31
CSK	20140810-20140826	2762	117	DESC	35.67	-77.63
CSK	20140810-20140830	2762	-93	DESC	35.67	-77.63
TSX	20120726-20140904	147-004	-394	ASC	23.97	74.94
RDS-2	20140808-20140901	34717 35060	-124	ASC	26.09	72.56

Supplementary Table 3: Interferograms
Interferograms formed through interferometric analysis of synthetic aperture radar (SAR) images, used for modelling the surface deformation in the vicinity of the dyke (COSMO-SkyMed (CSK) tracks 2631 and 2760, TerraSAR-X (TSX) orbit 147) as well as near the Bárðarbunga central volcano (CSK tracks 2761 and 2762). The RADARSAT-2 (RDS-2) interferogram is the only one covering both areas of interest, as shown in Fig. 1b and Extended Data Fig. 1. For each interferogram, the satellite is indicated as well as the dates of images used. The different time spans help constrain models of the space-time evolution of the dyke intrusion. Ascending and descending configurations were available for different time periods. The paths and their orbit numbers are detailed in the table. B_p stands for perpendicular baseline, the horizontal distance perpendicular to the satellite flight direction between the two repeat orbits.